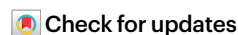


Microtubule-binding-induced allostery triggers LIS1 dissociation from dynein prior to cargo transport

Received: 23 November 2022

Accepted: 28 April 2023

Published online: 15 June 2023



William D. Ton^{1,3}, Yue Wang^{2,3}, Pengxin Chai^{2,3},
Cisloynny Beauchamp-Perez¹, Nicholas T. Flint¹, Lindsay G. Lammers¹,
Hao Xiong², Kai Zhang^{2,4}✉ & Steven M. Markus^{1,4}✉

The lissencephaly-related protein LIS1 is a critical regulator of cytoplasmic dynein that governs motor function and intracellular localization (for example, to microtubule plus-ends). Although LIS1 binding is required for dynein activity, its unbinding prior to initiation of cargo transport is equally important, since preventing dissociation leads to dynein dysfunction. To understand whether and how dynein–LIS1 binding is modulated, we engineered dynein mutants locked in a microtubule-bound (MT-B) or microtubule-unbound (MT-U) state. Whereas the MT-B mutant exhibits low LIS1 affinity, the MT-U mutant binds LIS1 with high affinity, and as a consequence remains almost irreversibly associated with microtubule plus-ends. We find that a monomeric motor domain is sufficient to exhibit these opposing LIS1 affinities, and that this is evolutionarily conserved between yeast and humans. Three cryo-EM structures of human dynein with and without LIS1 reveal microtubule-binding induced conformational changes responsible for this regulation. Our work reveals key biochemical and structural insight into LIS1-mediated dynein activation.

Cytoplasmic dynein-1 is a highly conserved molecular motor that transports cargos toward the minus-ends of microtubules. The dynein complex comprises several accessory chains and two copies of the ~500-kDa heavy chain, the latter of which possesses all of the elements required for motility¹. Processive motility requires that dynein first be released from an autoinhibited state, referred to as the ‘phi’ particle^{2–4}, and that it then associate with its activating complex dynactin and a cargo adapter that links dynein to dynactin and a variety of cargo^{5,6}.

A critical regulator of dynein is the lissencephaly-related protein LIS1 (also known as platelet-activating factor acetylhydrolase IB subunit beta, or PAFAH1B1), mutations in which lead to dynein dysfunction and severe neurodevelopmental disorders^{7,8}. Recent studies support a model whereby LIS1 binding to dynein prevents it from adopting the phi conformation^{2,7,9–11}. LIS1 has also been shown to promote dynein’s

association with microtubule plus-ends^{12–17}, and to aid in the recruitment of a second dynein complex to dynactin, thereby stimulating formation of faster motor complexes^{10,11,18,19}.

Although LIS1 binding to dynein is required for it to promote these activities, it is less clear whether LIS1 remains bound to dynein during cargo transport. Single-molecule motility assays have revealed varying extents of comigration of LIS1 with dynein. Whereas one study noted robust colocalization of LIS1 with motile dynein–dynactin–adapter (DDA) complexes (~75%)¹⁸, others have noted much lesser extents of binding (from ~15% to ~30% (refs. 2,10,11)), in spite of the large excess of LIS1 used in all these assays. Reconstitution of DDA behavior on dynamic microtubules revealed that LIS1 associates with and promotes plus-end binding of dynein (via EB1), but appears to dissociate prior to initiation of motility, since only a small fraction

¹Department of Biochemistry and Molecular Biology, Colorado State University, Fort Collins, CO, USA. ²Department of Molecular Biophysics and Biochemistry, Yale University, New Haven, CT, USA. ³These authors contributed equally: William D. Ton, Yue Wang, Pengxin Chai. ⁴These authors jointly supervised this work: Kai Zhang, Steven M. Markus. ✉ e-mail: jack.zhang@yale.edu; steven.markus@colostate.edu

of minus-end-directed DDA complexes possessed detectable LIS1 (ref. 20). This latter finding is consistent with data from budding yeast, in which overexpression of the dynein–dynactin-binding domain of the cargo adapter Num1 appears to promote assembly and motility of DDA complexes that do not colocalize with Pac1, the yeast homolog of LIS1 (ref. 21). Moreover, LIS1 homologs in filamentous fungi have been found to only transiently associate with retrograde-moving dynein-driven endosomes^{22,23}. Finally, although Pac1 associates with dynein at the plus-ends of microtubules in budding yeast, it does not colocalize with dynein at its site of activity in this organism: the cell cortex^{12,24}. Together, these data favor a model in which LIS1 and its homologs likely dissociate from dynein before initiation of cargo transport.

Whether dissociation of dynein from LIS1 is required for cargo transport in metazoa is unclear. However, one piece of evidence from budding yeast suggests that their dissociation is indeed crucial. Specifically, inclusion of bimolecular fluorescence complementation (BiFC) tags on Pac1 and Dyn1 (the latter of which encodes the dynein heavy chain) leads to a situation in which these two proteins remain associated following delivery of dynein–dynactin to cortical Num1 (owing to the irreversible association of the two split-YFP halves)^{25,26}. Whereas cells expressing only one of the two BiFC-tagged proteins possess normal dynein function, those expressing both exhibit defects in dynein function as severe as those cells lacking Dyn1, suggesting that dynein–Pac1 dissociation is critical for proper in-cell dynein activity.

Our understanding of LIS1 and Pac1 function is complicated by conflicting findings regarding these molecules' abilities to modulate dynein's microtubule-binding activity and its velocity. These data have suggested a model whereby Pac1 and LIS1 directly promote dynein's ability to remain associated with microtubule plus-ends^{27–29}. Arguments against this model include findings that a Pac1-bound dynein does not use its microtubule-binding domain (MTBD) to associate with plus-ends in cells²¹, and that the extent of Pac1's ability to reduce dynein velocity in vitro scales with Pac1's microtubule binding^{2,7}. Because Pac1 does not bind microtubules in cells^{12,25}, these findings force us to re-evaluate whether Pac1 and LIS1 actually impact dynein mechanochemistry. Determining whether LIS1 remains associated with motile dynein–dynactin complexes in cells will help to clarify these controversies.

Here, we set out to address the question of whether and how dynein–LIS1 affinity is modulated, and to determine whether microtubule binding by dynein may be responsible. We engineered dynein mutants constitutively locked in either a microtubule-unbound or microtubule-bound conformational state. Our data reveal that these mutants indeed reflect the native conformations of dynein in these two states, and that they have opposing affinities for LIS1. Specifically, the microtubule-unbound state of dynein exhibits higher affinity for LIS1 than does the microtubule-bound state. We find that the motor domain of dynein is sufficient for this behavior, and that it is conserved from yeast to humans. Cells expressing the microtubule-unbound

dynein mutant exhibit robust dynein–Pac1 binding, but little unbinding, and exhibit behavior consistent with an inability of dynein to dissociate from the plus-end-binding machinery, and thus the plus-ends themselves. Our observations indicate that dynein must switch to a microtubule-bound conformation to dissociate from LIS1, which then permits the adoption of a motility-competent state of the DDA complex. High-resolution cryo-electron microscopy (cryo-EM) structures reveal the structural basis for microtubule-binding-induced dissociation of dynein–LIS1. Our data are consistent with a model in which LIS1 must dissociate from dynein prior to initiation of cargo transport, and microtubule-binding is responsible for triggering this dissociation.

Results

Generation of microtubule-unbound and microtubule-bound dynein mutants

We have previously found that binding of the yeast cargo adapter protein Num1 to dynein–dynactin triggers dissociation of Pac1 from dynein, thus promoting minus-end-directed motility of the motor complex²¹. However, deletion of dynein's MTBD prevented this dissociation, suggesting that dynein must bind microtubules for this to occur. We thus sought to determine whether microtubule binding triggers dissociation of dynein from Pac1. Microtubule binding by dynein leads to a conformational change in the MTBD that is communicated to the AAA+ ring via a translation of the CC1 helix of the dynein stalk with respect to CC2, causing a change in the heptad registry of this coiled coil (Extended Data Fig. 1a)^{30–33}. We hypothesized that this helix shift initiates events that lead to dynein–Pac1 dissociation.

To test this, we used a previously employed protein-engineering strategy in which the dynein MTBD and short regions of CC1 and CC2 are replaced with a stable coiled coil derived from seryl transfer RNA (tRNA) synthetase (SRS_{CC})³⁴. By including or excluding four amino acids in CC1, sufficient to encode a single turn in this helix (Extended Data Fig. 1b), we aimed to lock CC1 in either an up or down state, thus reflecting the microtubule-bound or microtubule-unbound state, respectively³³. Consistent with previous work using *Dictyostelium discoideum* dynein³⁴, the microtubule-unbound (MT-U) and microtubule-bound (MT-B) mutants exhibit ATPase rates that closely match that of wild-type dynein in the absence and presence of microtubules, respectively (Extended Data Fig. 1c). As expected, neither mutant possesses microtubule-binding activity (Extended Data Fig. 1d).

Dynein mutants exhibit opposing localization behaviors

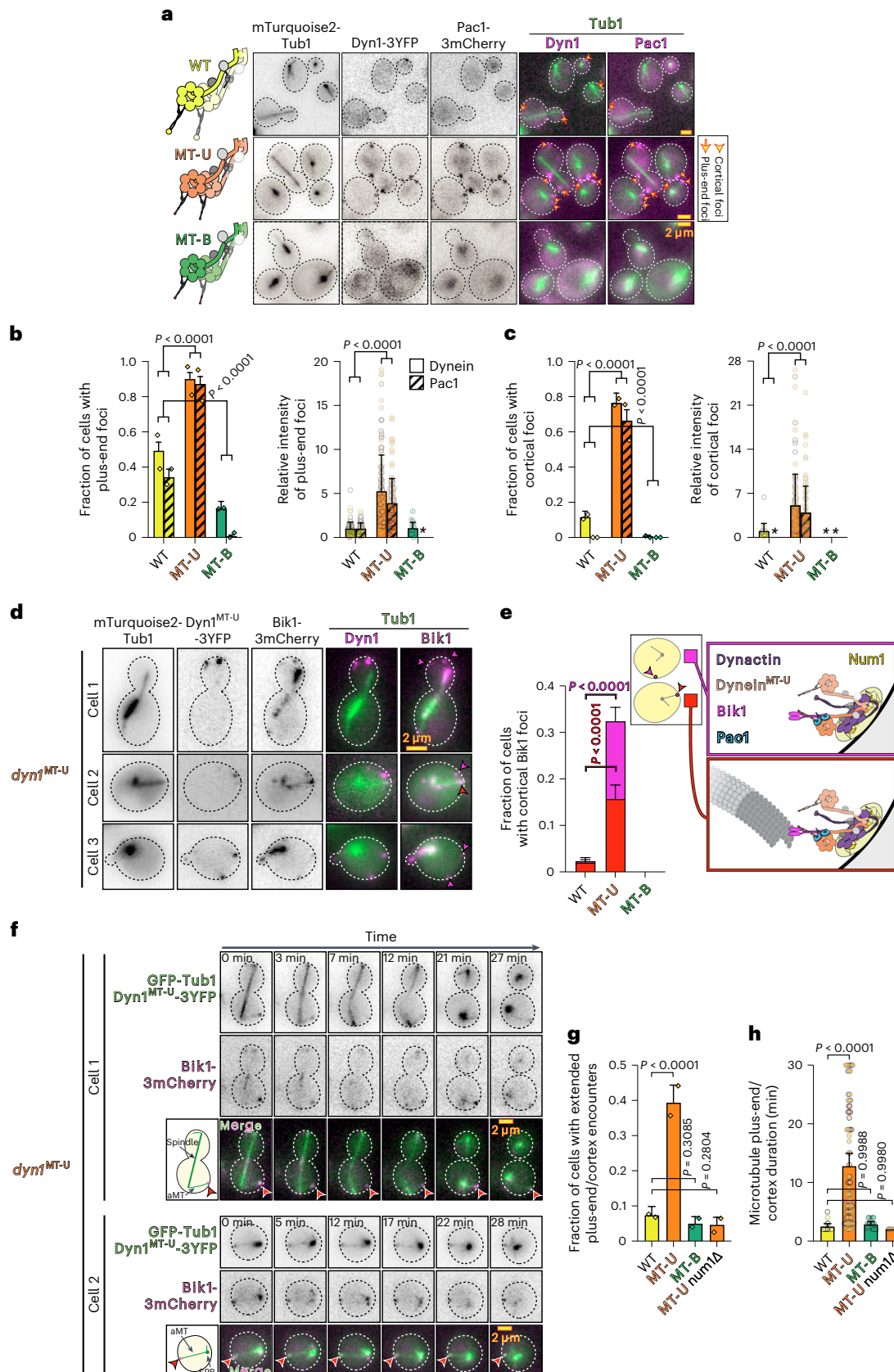
The extent to which dynein and Pac1 interact governs the degree to which these proteins localize to various sites in cells (for example, microtubule plus-ends). For instance, cells with no Pac1 exhibit an almost complete lack of dynein foci^{12,17}, whereas those overexpressing Pac1 or expressing a dynein mutant with higher-than-wild-type affinity for Pac1 both exhibit a greater number of dynein foci^{2,24,25}. Thus, the number and

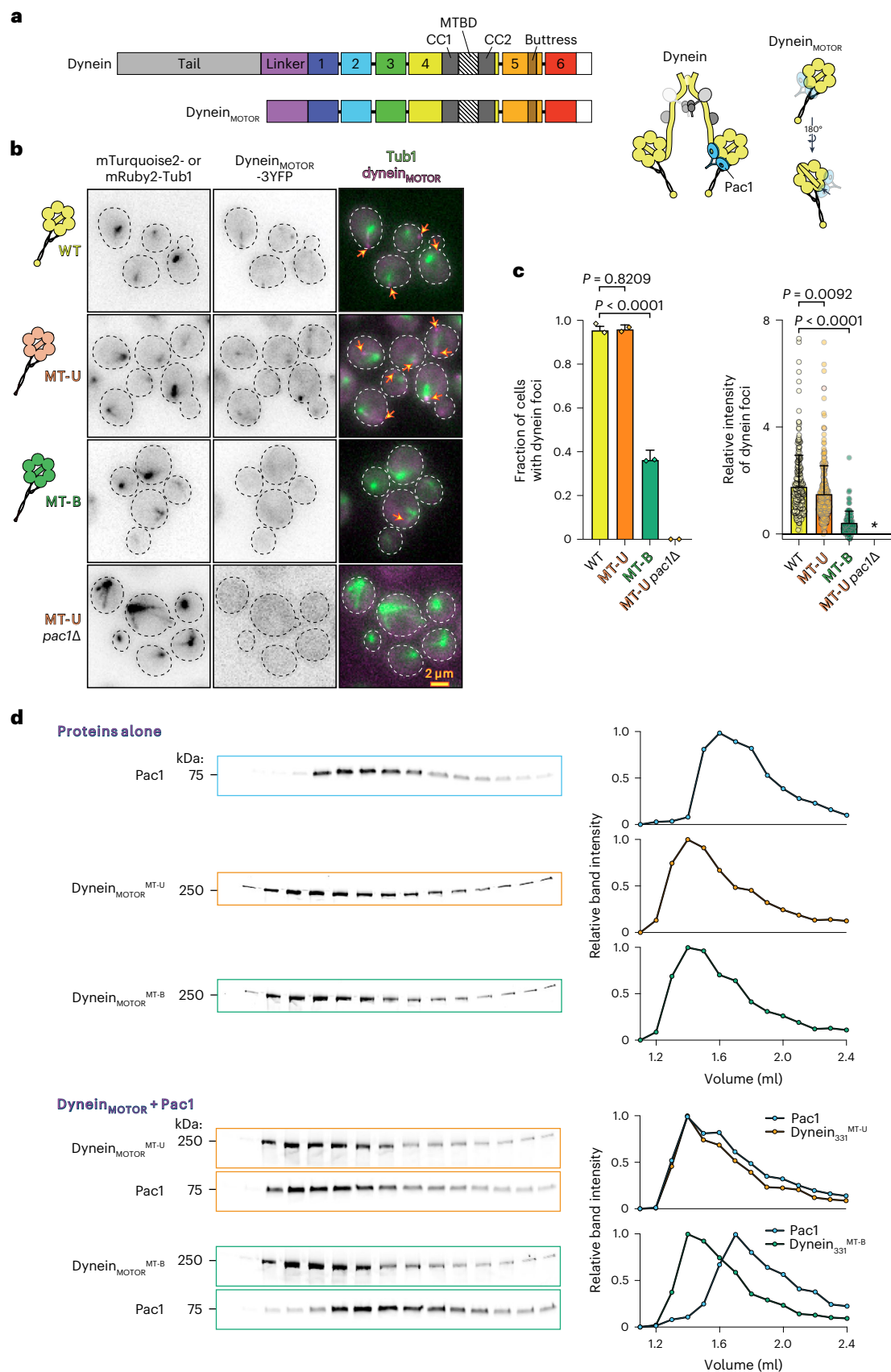
Fig. 1 | The microtubule-unbound dynein mutant is tightly bound to Pac1, Bik1, and microtubule plus-ends in cells. **a**, Representative images of cells expressing Pac1-3mCherry, mTurquoise2-Tub1, and either Dyn1^{MT-U}-3YFP or Dyn1^{MT-B}-3YFP. **b,c**, Plots (mean \pm s.d., along with all data points) depicting frequency and relative intensity of plus-end (**b**) and cortical (**c**) dynein and Pac1 foci in cells expressing the indicated *DYN1* allele as the only source of dynein heavy chain (WT, wild-type; MT-U, microtubule-unbound mutant; MT-B, microtubule-bound mutant; *, no foci observed; $n = 101/25$ plus-end/cortical dynein foci, and 73/0 plus-end/cortical Pac1 foci from 213 *DYN1* cells; 114/108 plus-end/cortical dynein foci, and 116/87 plus-end/cortical Pac1 foci from 110 *dyn1*^{MT-U} cells; 24/0 plus-end/cortical dynein foci, and 1/0 plus-end/cortical Pac1 foci from 147 *dyn1*^{MT-B} cells; all from 2 biological replicates). **d**, Representative images of cells expressing Bik1-3mCherry, mTurquoise2-Tub1, and Dyn1^{MT-U}-3YFP (magenta arrowheads, cortical Bik1 foci without associated plus-ends; red arrowhead, cortical Bik1 focus with associated plus-end). **e**, Plot (mean \pm s.d.) depicting the frequency of cells with the indicated dynein allele possessing

cortical Bik1 foci (either with or without the associated microtubule plus-end, as indicated; $n = 305, 281$, and 226 *DYN1*, *dyn1*^{MT-U}, and *dyn1*^{MT-B} cells, respectively, from 2 independent replicates). **f**, Representative time-lapse images of cells expressing Bik1-3mCherry, GFP-Tub1, and Dyn1^{MT-U}-3YFP (arrowheads, instances of plus-ends with Bik1 foci statically associated with the cortex for 27–28 min). Cartoons represent cell in first frame of movie (aMT, astral microtubule; SPB, spindle pole body; magenta circles, plus-end Bik1 foci statically associated with cortex). Also see Supplementary Video 1. **g,h**, Plots (mean \pm s.d., along with all data points) depicting frequency (**g**) and duration (**h**) of extended plus-end-cortex encounters (those lasting ≥ 2 min) in cells with the indicated dynein and/or Num1 allele ($n = 15$ events from 206 *DYN1* cells, 74 events from 188 *dyn1*^{MT-U} cells, 12 events from 241 *dyn1*^{MT-B} cells, and 8 events from 173 *dyn1*^{MT-U} *num1* Δ cells, all from 2 independent replicates; cells used in **f–h** are distinct biological isolates from those used in **d** and **e**). Two-tailed *P* values were calculated from *Z* scores for proportion data, or by comparing means using a Dunnett's test (for intensity values and microtubule-cortex duration values).

brightness of dynein foci directly correlate with dynein–Pac1 affinity. Imaging cells expressing Pac1-3mCherry and either dynein^{MT-U}-3YFP or dynein^{MT-B}-3YFP revealed that these two mutants exhibit opposing degrees of localization. Specifically, dynein^{MT-U}-expressing cells

exhibit more plus-end and cortical dynein foci than wild-type cells, while only a small fraction of dynein^{MT-B}-expressing cells exhibit foci. Moreover, intensity measurements revealed that dynein^{MT-U} foci were much brighter than dynein^{MT-B} foci (Fig. 1a–c, non-hatched bars).





The pattern of Pac1 localization in these cells reflects that of the respective dyneins (Fig. 1a–c, hatched bars). Whereas neither wild-type nor *dyn1*^{MT-B} cells (the latter being those expressing dynein^{MT-B}) possess Pac1 foci at the cell cortex, a large fraction of *dyn1*^{MT-U} cells do,

almost all of which colocalize with dynein^{MT-U} (Fig. 1a,c). Given that Pac1 is never observed at the cortex in wild-type cells, we wondered whether Bik1 (homolog of human CLIP-170) also localizes to cortical sites in *dyn1*^{MT-U} cells. Bik1 is required for plus-end association of

Fig. 2 | The dynein motor domain is sufficient for microtubule-binding-induced allostery. **a**, Schematic (left) and cartoon depictions (right) of full-length dynein and the truncated dynein motor domain (CC, coiled-coil; MTBD, microtubule-binding domain). The arrow on the cartoon indicates the truncated dynein linker that does not contact Pac1 (ref. 27). Note the truncated motor domain lacks the tail domain, which is required for Num1 and dynactin binding³⁵. **b**, Representative fluorescence images of cells expressing mTurquoise2-Tub1 (for all strains except *dyn1^{MOTOR}MT-U**pac1Δ*) or mRuby2-Tub1 and indicated dynein motor domain fragment (arrows, plus-end foci). **c**, Plots (mean \pm s.d., with means from each replicate indicated by diamonds on fraction plots, or differently shaded circles for all data points on intensity plots) depicting frequency and

relative intensity of dynein foci, which were scored from time-lapse movies ($n = 278$ foci from 196 wild-type *dyn1^{MOTOR}* cells; 240 foci from 194 *dyn1^{MOTOR}MT-U* cells; 97 foci from 224 *dyn1^{MOTOR}MT-B* cells; 0 foci from 251 *dyn1^{MOTOR}MT-U* *pac1Δ* cells; all from 2 biological replicates). All intensity values were normalized to the mean values (for each replicate) for dynein_{MOTOR}-3YFP in wild-type cells (set to 1). Two-tailed P values were calculated from Z scores (for proportion data) or by comparing means using a Dunnett's test (for intensity values). **d**, Analytical size-exclusion chromatography analysis showing each protein alone (top) or mixtures of both proteins (bottom) run on a Superdex 5/150 (bottom). Plots depict band intensity profiles. Gels and accompanying analyses are representative of at least three independent replicates.

dynein and Pac1, and makes a tripartite complex with these proteins at plus-ends^{17,24,25}. Imaging *dyn1^{MT-U}* cells expressing Bik1-3mCherry revealed that this protein also ectopically localizes to cortical sites (Fig. 1d). Whereas some cortical Bik1 foci were not associated with microtubules (magenta arrowheads and bars in Fig. 1d,e), others were simultaneously associated with the cortex and a microtubule plus-end (red arrowheads and bars). Time-lapse imaging revealed that plus-ends remain anchored at cortical sites in *dyn1^{MT-U}* cells for much longer than in wild-type or *dyn1^{MT-B}* cells, with some lasting throughout the entire 30-minute imaging period (Fig. 1f–h and Supplementary Video 1). We confirmed the plus-ends were anchored via canonical cortical dynein complexes by deleting Num1, which resulted in a large reduction in these events (Fig. 1g,h).

These data indicate that dynein is in a microtubule-unbound conformation at plus-ends, and that it must switch to a microtubule-bound state to dissociate from Pac1. Failure to do so results in dynein remaining bound to Pac1 and the microtubule plus-end via Bik1.

Allostery within dynein motor domain governs Pac1 affinity

To determine the minimal region of dynein that is sufficient to exhibit differential Pac1 affinity, we assessed the localization of a motor domain truncation (Fig. 2a). This region (dynein_{MOTOR}), which encompasses the AAA+ ring and most of the linker element, is sufficient for Pac1 binding and thus for localizing to plus-ends³⁵. This fragment is missing a region of the linker that has previously been found to encounter Pac1 during its powerstroke (arrow, Fig. 2a, right)²⁷. Whereas the extent of plus-end binding by dynein_{MOTOR}^{MT-U}-3YFP is similar to that of wild-type dynein_{MOTOR}, dynein_{MOTOR}^{MT-B}-3YFP was present in fewer cells, and with a lower fluorescence intensity (Fig. 2b,c). Thus, the structural determinants that account for differential Pac1 affinity are contained within the motor domain.

To determine whether dynein and Pac1 are sufficient to exhibit this behavior in vitro, we combined purified dynein_{MOTOR} and Pac1, and applied them to a size-exclusion chromatography column. Pac1 comigrated with dynein_{MOTOR}^{MT-U} to a greater extent than dynein_{MOTOR}^{MT-B}, indicating that Pac1 binds dynein_{MOTOR}^{MT-U} with greater affinity than dynein_{MOTOR}^{MT-B} (Fig. 2d).

Fig. 3 | Mass photometric analysis of Pac1–dynein_{MOTOR} binding. **a**, Proteins purified from yeast were diluted into assay buffer without nucleotide, and videos were acquired on a Refeyn TwoMP thereafter. The masses of protein species landing on the glass coverslip were empirically determined by converting particle contrast to mass following a calibration routine in the Refeyn software. Fitting of raw data, which identifies mean mass values for each species and reveals the relative fraction of particles with indicated mass, was performed in Discover MP. The data reveal that the majority of Pac1 exists as a dimer, whereas the motor domains are mostly monomeric. **b,c**, Histograms depicting relative fraction of unbound Pac1, unbound dynein_{MOTOR} (MT-U or MT-B), or bound dynein_{MOTOR}–Pac1 complexes. Equimolar concentrations of Pac1 and either dynein_{MOTOR}^{MT-U} (**b**) or dynein_{MOTOR}^{MT-B} (**c**; 25 nM each) were mixed in an assay buffer with the indicated nucleotide (1 mM), incubated for 1–2 minutes, and then

To validate these findings, we employed mass photometry, a microscopy-based single-molecule method that permits determination of the masses of protein species within a mixture³⁶. Analysis of the proteins alone revealed that the large majority of each had mass values consistent with dimeric Pac1 and monomeric dynein_{MOTOR} (Fig. 3a and Extended Data Fig. 2a). We then mixed Pac1 with each dynein_{MOTOR} fragment and assessed the proportion of species that resulted. In the presence of ATP, we noted an approximately twofold greater proportion of dynein_{MOTOR}^{MT-U}–Pac1 complexes (see ~520-kDa peak) than dynein_{MOTOR}^{MT-B}–Pac1 complexes (Fig. 3b–d). This was true across a range of Pac1 concentrations (Extended Data Fig. 2b). This experiment also revealed that wild-type dynein_{MOTOR} bound to Pac1 with an affinity that was almost identical to dynein_{MOTOR}^{MT-U} (Fig. 3d and Extended Data Fig. 2a), which is consistent with the notion that this mutant mimics wild-type microtubule-unbound dynein.

The nucleotide-bound state of dynein affects Pac1 affinity

Previous studies have found that dynein–LIS1 binding is enhanced by treatment with ATP and vanadate²⁹, which results in an ADP–Pi-like state³⁷. To determine how different nucleotides affect the ability of MT-U or MT-B to bind Pac1, we repeated our mass photometry experiments with either no nucleotide ('apo'), AMPPNP (non-hydrolyzable ATP), ATP and vanadate (Vi), or ADP. As expected, ADP–Vi indeed enhances Pac1 binding for both wild-type dynein_{MOTOR} and dynein_{MOTOR}^{MT-U} (Fig. 3b–d and Extended Data Fig. 2a); however, Pac1–dynein_{MOTOR}^{MT-B} binding is unaffected by ADP–Vi. AMPPNP also strongly enhances Pac1 binding to dynein_{MOTOR} and dynein_{MOTOR}^{MT-U}, but has only a minor effect on dynein_{MOTOR}^{MT-B}. Interestingly, apo conditions led to a situation in which all three dynein_{MOTOR} fragments bound to Pac1 with similar affinities. Finally, ADP has a minor enhancing effect for Pac1 binding to all three fragments. Given the similar response of dynein_{MOTOR} and dynein_{MOTOR}^{MT-U} in all conditions, these data further support the notion that these two fragments are structurally and biochemically similar, whereas the dynein_{MOTOR}^{MT-B} mutant is distinct, and may represent the bona fide microtubule-bound state of dynein (see Supplementary Results).

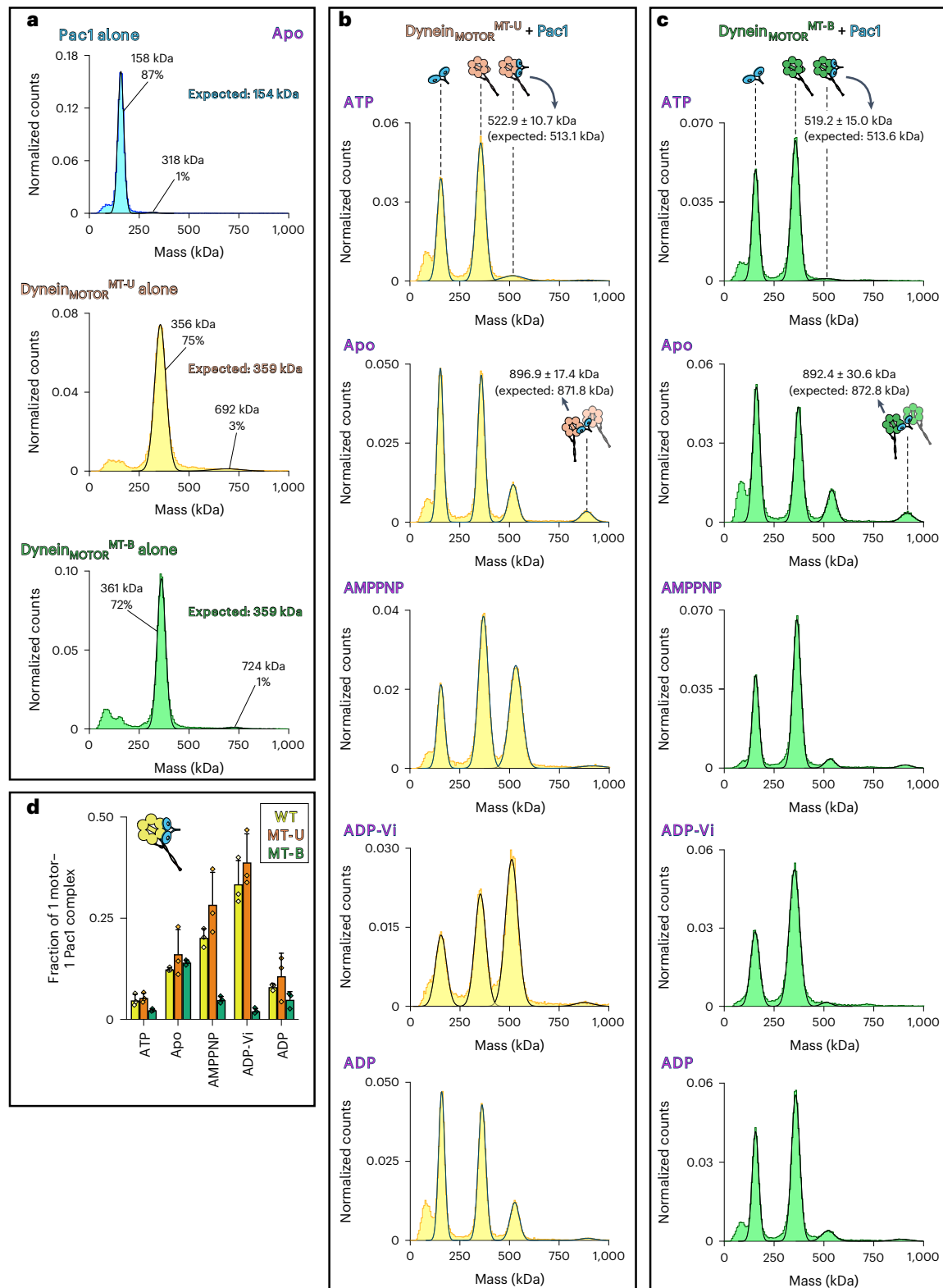
In light of the inability of ADP–Vi to affect the Pac1-binding affinity of dynein_{MOTOR}^{MT-B}, we wondered whether this mutant can bind

diluted to 5 nM on a coverslip mounted on a Refeyn TwoMP. Videos were acquired immediately thereafter, and mass analysis was performed using Discover MP. Particles within the 523-kDa peak correspond to 1 Pac1 dimer–1 dynein_{MOTOR} monomer complexes; those within the 897-kDa peak likely correspond to 1 Pac1 dimer–2 dynein_{MOTOR} complexes (see cartoon schematic above each peak). Plots depict representative data of at least three independent replicates. **d**, The relative fraction of 1 Pac1 dimer–1 dynein_{MOTOR} monomer complexes are plotted (mean \pm s.d., along with all data points). See Extended Data Fig. 2b for representative mass histograms with the wild-type dynein_{MOTOR} protein with and without Pac1 ($n = 3$ independent replicates each). Note that we observed a smaller fraction of dynein_{MOTOR}–Pac1 complex formation when we used mass photometry than in our analytical gel filtration data (Fig. 2d). This is likely a consequence of the lower concentrations needed for mass photometry (~20-fold difference; see Methods).

Vi. To address this, we mixed the dynein_{MOTOR} fragments with ATP in the absence or presence of Vi, and exposed them to ultraviolet light. Although wild-type and dynein_{MOTOR}^{MT-U} underwent Vi-dependent photocleavage, indicative of Vi binding to AAA1, dynein_{MOTOR}^{MT-B} did not, indicating that the microtubule-bound conformation has a low affinity for Vi (and by extension, Pi; Extended Data Fig. 3). Thus, treatment with ATP and Vi does not enhance the Pac1-binding affinity of dynein_{MOTOR}^{MT-B} because it is unable to bind Vi (see Supplementary Discussion).

Allostery governing LIS1 affinity is conserved in humans

To determine whether the phenomenon we have described thus far is conserved in human proteins, we purified LIS1 and corresponding human dynein_{MOTOR} fragments from insect cells, and assessed their binding via mass photometry. This revealed a very similar difference in LIS1-binding affinity between the two mutants in ATP (Fig. 4b–d). Repeating the binding experiments in the presence or absence of different nucleotides revealed an almost identical response of the human



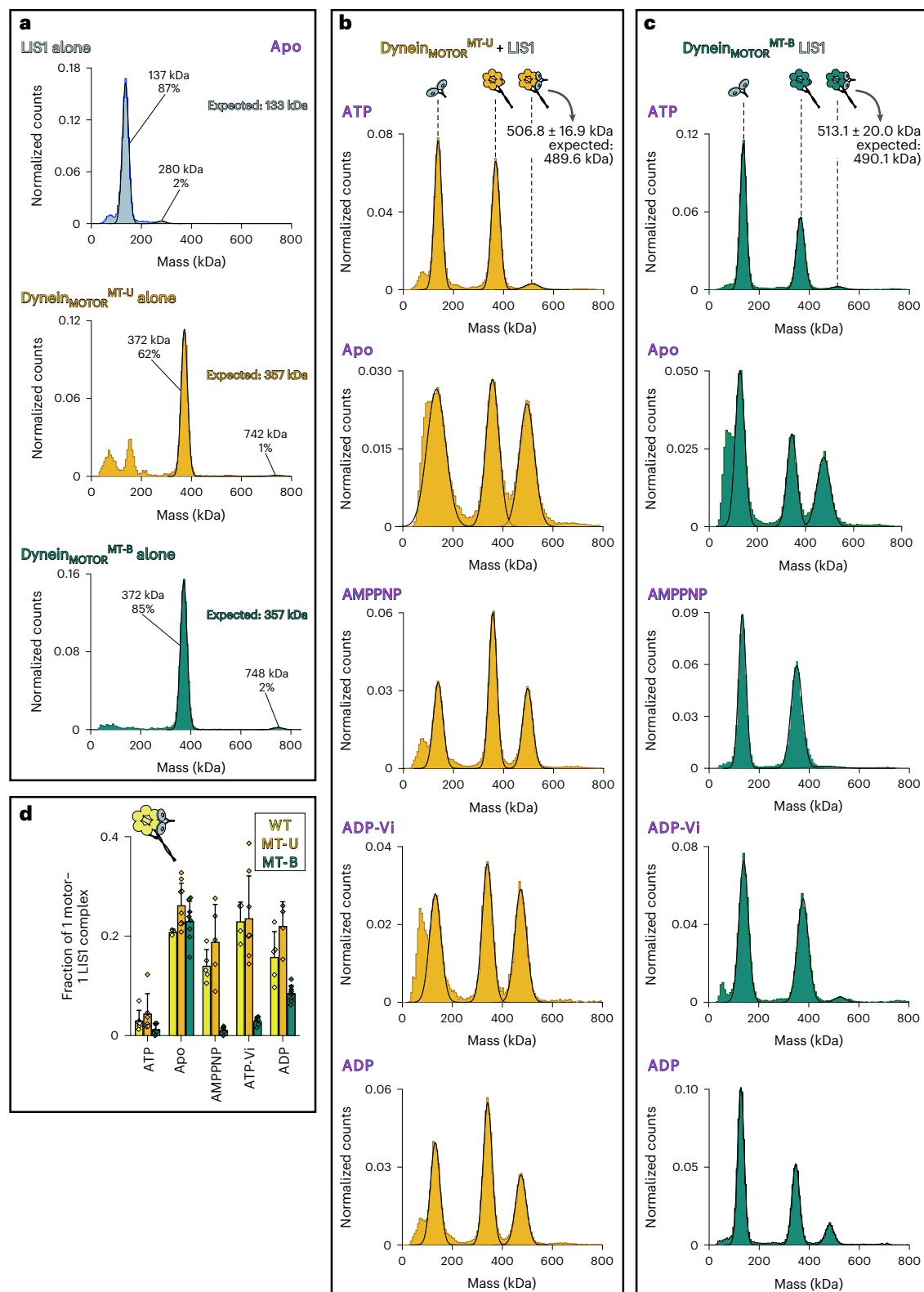


Fig. 4 | Mass photometric analysis of human LIS1–dynein_{MOTOR} binding.

a, Proteins purified from insect cells were diluted in assay buffer without nucleotide, and videos were acquired on a Refeyn TwoMP as described in Figure 3. The data reveal that the majority of LIS1 exists as a dimer, whereas the motor domains are mostly monomeric. **b, c**, LIS1 and either human dynein_{MOTOR}^{MT-U} (**b**) or dynein_{MOTOR}^{MT-B} (**c**) were mixed in assay buffer with the indicated nucleotide (to 25 nM each), incubated for 1–2 min, and then diluted to 5 nM on the Refeyn TwoMP. Videos were acquired immediately thereafter, and mass analysis was performed using Discover MP. Particles within the 507-kDa peak correspond to 1 LIS1

dimer–1 dynein_{MOTOR} monomer complexes (see cartoon schematic above each peak). We did not observe protein species corresponding to the 1 LIS1 dimer–2 dynein_{MOTOR} complexes observed with yeast proteins in Figure 3. Plots depict representative data for at least three independent replicates. **d**, The relative fraction of 1 LIS1 dimer–1 dynein_{MOTOR} monomer complexes are plotted (mean ± s.d., along with all data points). See Extended Data Fig. 2c for representative mass histograms with the wild-type human dynein_{MOTOR} protein with and without LIS1 (from left to right, $n = 6/6/5$, $3/9/8$, $5/5/6$, $4/8/6$, and $5/4/9$ independent replicates).

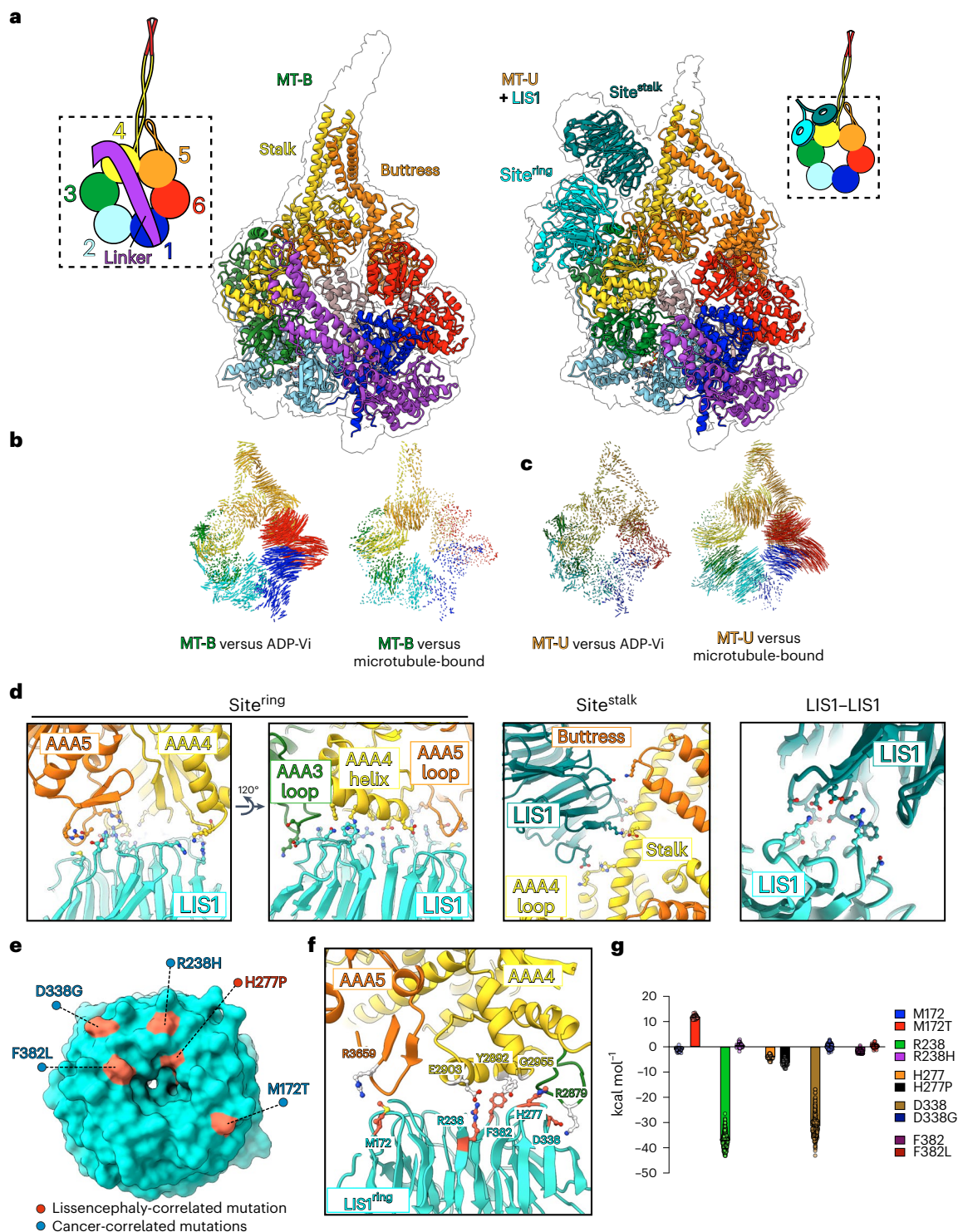


Fig. 5 | Cryo-EM structures of human dynein_{MOTOR}^{MT-B} and a LIS1-bound dynein_{MOTOR}^{MT-U}. **a**, Molecular models of dynein_{MOTOR}^{MT-B} (solved in the presence of ATP) and LIS1-bound dynein_{MOTOR}^{MT-U} (solved in the presence of ATP and Vi) with corresponding density maps (indicated with outlines). Subdomains are color-coded, as indicated by cartoon. **b,c**, Vector maps depicting pairwise alpha carbon interatomic distances between dynein_{MOTOR}^{MT-B} (**b**) or dynein_{MOTOR}^{MT-U} (**c**) with either the human ADP-Vi-bound dynein-2 crystal structure (4RH7)³⁷, or the native microtubule-bound dynein-1 cryo-EM structure (7Z8G)³⁸. Structures were globally aligned after removal of the linkers. The length of the lines are proportional to the calculated interatomic distances. Note the strong similarities between dynein_{MOTOR}^{MT-B} and the microtubule-bound dynein (but not with the human ADP-Vi-bound dynein-2 crystal structure), and that of dynein_{MOTOR}^{MT-U} with

the ADP-Vi-bound dynein (but not with the native microtubule-bound dynein-1 cryo-EM structure). **d**, Close-up views of the main contact points between LIS1 and either site^{ring} or site^{stalk} (as indicated), and between the two LIS1s within the homodimer. Also see Supplementary Video 2. Residues with atoms shown are those determined to mediate contacts (see Extended Data Fig. 6b). **e**, Surface view showing site^{ring}-bound LIS1, with disease-correlated residues highlighted. **f**, Close-up view of contact points between disease-correlated residues on LIS1 and site^{ring}. **g**, Plot (mean \pm s.d., along with all data points) depicting results of MD simulations, showing the energy of interaction between LIS1 and either wild-type or mutant dynein, as indicated (from left to right, $n = 40, 43, 256, 46, 41, 46, 243, 81, 84$, and 46 iterations). See Extended Data Fig. 6d for graphical depiction of MD simulation data.

Table 1 | Cryo-EM data collection, refinement, and validation statistics

Description	MT-B, full map (EMD-2899), (PDB 8FCY)	MT-U, full map (EMD-29003), (PDB 8FD6)	MT-U + 2 LIS1s, full map (EMD-29012), (PDB 8FDT)	MT-U + 2 LIS1, AAA3-AAA5+2 LIS1s, local refined map (EMD-29014), (PDB 8FDU)
Data collection and processing				
Microscope	Glacios	Glacios	Titan Krios	
Voltage (kV)	200	200	300	
Camera	K2	K2	K3	
Magnification	36,000	36,000	105,000	
Pixel size (Å)	1.149	1.149	0.825	
Total Electron Exposure (e ⁻ /Å ²)	40	40	50	
Defocus range (μm)	1.5–2.7	1.5–2.7	1.5–2.7	
Symmetry imposed	C ₁	C ₁	C ₁	
Initial particles	250,463	729,028	1,400,918	
Final particles	44,752	201,707	53,572	
Refinement				
Initial models	5NUG	5NUG	5NUG, 7MGM, AlphaFold	5NUG, 7MGM, AlphaFold
Map pixel size	1.149	1.149	1.149	1.149
Map resolution (FSC 0.143)	3.4	2.9	3.2	3.2
Map resolution (3D FSC)	3.5	3.0	3.4	3.4
Map resolution range (Å)	3.1–10	2.8–10	3.0–10	3.0–10
Map sharpening B-factor (Å ²)	−56	−64	−44	−52
Model composition				
Non-hydrogen atoms	23,157	22,182	27,103	13,189
Protein residues	2,866	2,749	3,370	1,633
Ligands	ATP (1)/ADP (3)	ATP (1)/ADP (3) VO ₄ (1)/Mg ²⁺ (1)	ATP (1)/ADP (3) VO ₄ (1)	ADP (2)
Model versus data				
FSC map to model (FSC 0.5)	3.7	3.2	3.7	3.6
Correlation coefficient (mask)	0.86	0.80	0.80	0.79
B factors (Å ²)				
Protein	95.89	79.10	87.63	101.23
Nucleotide	77.44	59.87	56.36	76.23
R.m.s. deviation				
Bond length (Å)	0.002	0.006	0.003	0.004
Bond angles (°)	0.549	0.671	0.607	0.680
Validation				
Molprobtity score	1.74	1.76	1.80	1.87
Clashscore	7.86	9.20	10.91	12.64
Rotamer outliers (%)	0.08	0.00	0.00	0.00
Ramachandran plot				
Outliers (%)	0.04	0.00	0.06	0.00
Allowed (%)	4.45	3.95	3.58	3.75
Favored (%)	95.52	96.05	96.36	96.25
Rama-Z (whole)	0.50	0.43	0.69	−0.17

proteins to LIS1 binding as the yeast proteins (Fig. 4d and Extended Data Fig. 2c). The only notable differences between the yeast and human proteins were a somewhat stronger enhancement of LIS1 binding for both mutants by the apo state, and a more pronounced stimulation by ADP. These data indicate that microtubule-binding-induced conformational changes also reduce the affinity of human dynein for LIS1.

Cryo-EM structures of human MT-B and LIS1-bound MT-U dynein

Our data thus far indicate that dynein_{MOTOR}^{MT-U} behaves almost identically to wild-type dynein with respect to LIS1 binding, but that dynein_{MOTOR}^{MT-B} exists in a low-LIS1-affinity state. To determine the structural basis for this behavior, we obtained 3.4- and 3.2-Å cryo-EM structures for human dynein_{MOTOR}^{MT-B} alone and a LIS1-bound dynein_{MOTOR}^{MT-U}, respectively (Fig. 5a, Extended Data Fig. 4a–j, and Table 1). While dynein_{MOTOR}^{MT-B} was

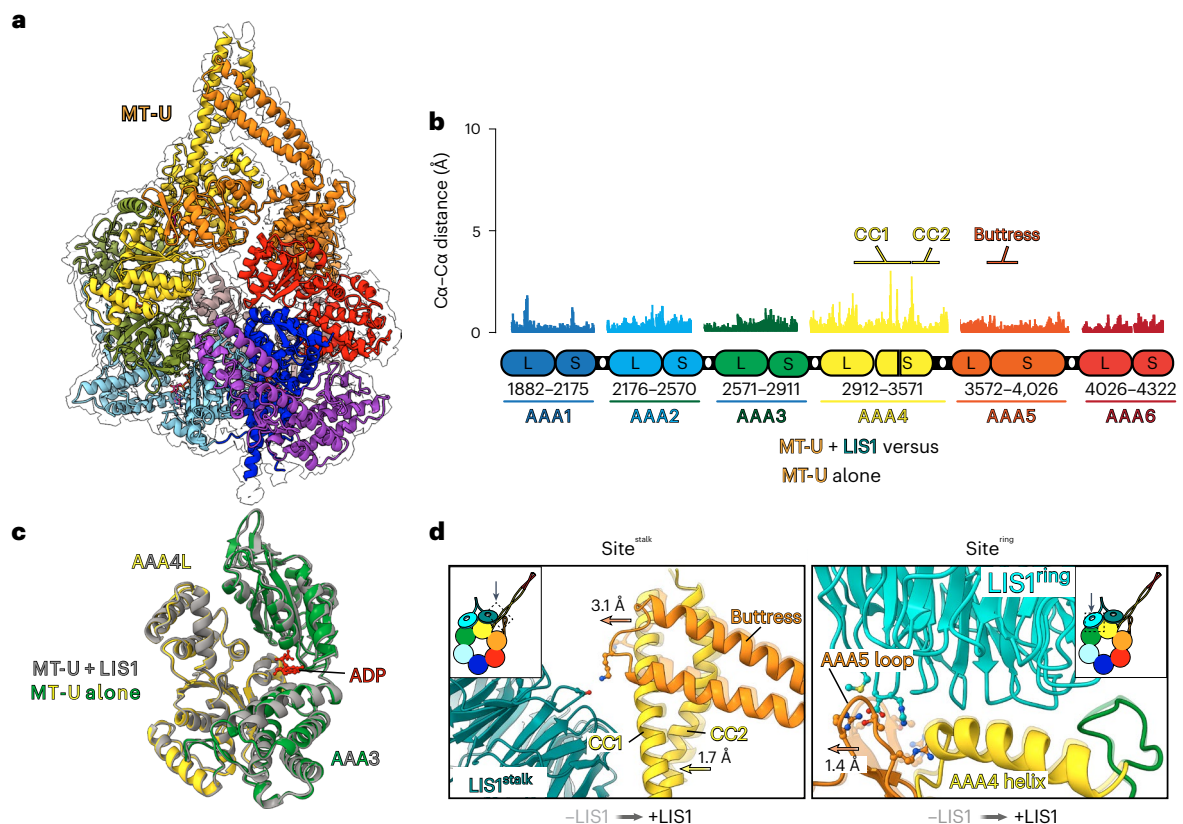


Fig. 6 | Cryo-EM structure of human dynein_{MOTOR}^{MT-U} alone. **a, Molecular model of dynein_{MOTOR}^{MT-U} (solved in the presence of ATP and Vi) with corresponding density map (indicated with outline). Subdomains are color-coded as indicated by cartoon shown in Figure 5a. **b**, Plot depicting pairwise alpha carbon interatomic distances between the dynein_{MOTOR}^{MT-U} with and without LIS1. L, large AAA subdomain; S, small AAA subdomain. Note the high degree of similarity between the two structures, with minor exceptions in CC1 and CC2 (see text).**

c, AAA3-AAA4L domains from dynein_{MOTOR}^{MT-U} with (gray) and without LIS1 (green and yellow) overlaid to depict the high degree of structural similarity. **d**, Close-up views illustrating the differences in dynein structure with and without LIS1 at the contact points between dynein and LIS1. The structure without LIS1 is depicted with reduced opacity compared with that with LIS1. Note the small shifts in the buttress tip toward site^{stalk}-bound LIS1 and of the AAA5 loop away from site^{ring}-bound LIS1.

frozen in the presence of ATP, we froze dynein_{MOTOR}^{MT-U} in the presence of ATP and Vi to enrich LIS1-bound complexes. We were able to unambiguously assign nucleotide densities to all four binding pockets in both dyneins (Extended Data Fig. 5a,e). Although ADP-Vi was apparent in the AAA1 pocket of dynein_{MOTOR}^{MT-U}, that of dynein_{MOTOR}^{MT-B} was bound to ADP, suggesting that the microtubule-bound state of dynein has a high affinity for ADP at AAA1. This is consistent with a recent report in which ADP was observed at AAA1 for a native microtubule-bound dynein–dynactin–adapter complex³⁸.

Comparisons to published structures revealed varying degrees of similarity (Fig. 5b,c, Extended Data Fig. 5b,c,g, and Supplementary Table 1). Notably, that which most closely resembles dynein_{MOTOR}^{MT-B} is the native microtubule-bound dynein described above. The minor differences between these two structures can be accounted for by the presence of AMPPNP instead of ADP at AAA3 in the native microtubule-bound dynein (Extended Data Fig. 5d). Consistent with our data indicating that dynein_{MOTOR}^{MT-U} behaves like wild-type dynein in the absence of microtubules, its structure very closely resembles that of the ADP-Vi-bound dynein-2 (Fig. 5c and Supplementary Table 1). These data indicate that our mutants indeed reflect microtubule-unbound and microtubule-bound conformations, and that the latter is distinct from the conformation adopted by a microtubule-unbound dynein in the presence or absence of various nucleotide analogs.

Our dynein_{MOTOR}^{MT-U}–LIS1 structure revealed that the monomeric motor bound to two LIS1 WD40 beta-propellers (Fig. 5a). Given that our mass photometry data indicate a 1:1 binding stoichiometry

(1 LIS1 dimer:1 dynein motor), these two beta-propellers are likely from the same LIS1 homodimer (Extended Data Fig. 6a,c). Consistent with previous structures of yeast dynein bound to a Pac1 dimer^{39,40}, the LIS1 beta-propellers were bound to two sites on the human dynein motor: one at the interface of AAA3 and AAA4 (referred to as site^{ring}), and the other at the base of the stalk (site^{stalk}). Binding of LIS1 to site^{ring} involves a surface-exposed helix in AAA4, a short loop within AAA5, and part of a longer loop within AAA3, while binding at site^{stalk} involves residues along the stalk, part of a long loop within AAA4, and residues at the tip of the buttress (Fig. 5d, Extended Data Figs. 6b and 7, and Supplementary Video 2). We also noted contacts between the two LIS1 beta-propellers. All of these contacts are consistent with those identified in a recent structure of a yeast dynein–Pac1 complex³⁹, and also with a very recent structure of wild-type human dynein bound to LIS1⁴¹ (Extended Data Fig. 6b, Supplementary Fig. 1, and Supplementary Table 1), further supporting the notion that dynein_{MOTOR}^{MT-U} reflects the native microtubule-unbound dynein.

Inspection of the LIS1 regions that contact site^{ring} and site^{stalk} revealed numerous residues distributed over the face of the two beta-propellers (Extended Data Figs. 6b and 8, and Supplementary Video 2). Although one of these residues (H277) has been found to be mutated in a person with lissencephaly⁴², four others have been found to be mutated in people with cancer (Fig. 5e,f; p.M172T, p.R238H, p.D338G, and p.F382L)⁴³. We used molecular dynamics (MD) simulations to analyze the potential consequences of these alterations on the dynein–LIS1 interaction, and found that the cancer-correlated

alterations all decrease the energy of interaction to varying degrees, while the lissencephaly-correlated substitution did not (Fig. 5g and Extended Data Fig. 6d). These data suggest that weakened LIS1–dynein interactions caused by p.M172T, p.R238H, p.D338G, or p.F382L may be linked to tumorigenesis.

An analysis of our dynein_{MOTOR}^{MT-U}–LIS1 cryo-EM dataset revealed that a subset of these dyneins were bound to only 1 LIS1 (36%), while the remaining were either bound to 2 (29%) or ‘1.5’ molecules (34%), in which a strong density was apparent for only one of the LIS1 molecules, with a weaker density corresponding to the second LIS1, which is indicative of flexibility of the latter molecule (Extended Data Fig. 4f). All LIS1-bound dyneins possess clear density at site^{ring}, indicating this is the primary binding site, while the presence of the site^{stalk}-bound LIS1 was variable, suggesting that this site is the lower affinity LIS1-binding site on dynein. Local resolution analysis of the three classes revealed that the density for the site^{ring}-bound LIS1 is best for the 1.5 and 2 LIS1-bound dyneins (as determined by the resolution of the bound LIS1; Extended Data Fig. 9a). Moreover, all three classes exhibit clear density for ADP within the AAA3 binding pocket, suggesting that nucleotide state does not cause these differences (Extended Data Fig. 9b). These observations suggest that the binding of LIS1 to site^{stalk}, which appears to be rate-limiting, stabilizes the entire LIS1 dimer–dynein complex. In addition to the improved resolution of LIS1, we also noted that two regions at site^{stalk} also exhibit greater resolution when more than 1 LIS1 is present: the AAA4 loop (residues 3111–3138), and the tip of the buttress, suggesting these regions become less flexible when bound to LIS1 (Extended Data Fig. 9b).

Cryo-EM structure of human MT-U dynein without LIS1

The reduced flexibility of the LIS1-binding regions of dynein, as well as previously published work, suggest that LIS1 binding may affect the conformation of dynein^{28,40}. It remains controversial whether this binding affects dynein’s mechanochemistry and/or microtubule-binding behavior⁷. We reasoned that if LIS1 were to impact the biochemical behavior of dynein, its binding would cause structural changes reflective of these activities. To determine whether this is the case, we solved a 2.9-Å cryo-EM structure of dynein_{MOTOR}^{MT-U} in the absence of LIS1, but in the presence of ATP and Vi (to allow an accurate comparison with the LIS1-bound dynein). With a few exceptions, this revealed a structure that was almost identical to that of the LIS1-bound dynein_{MOTOR}^{MT-U} (Fig. 6a,b). Notably, the conformation of the nucleotide binding pocket at AAA3, which was clearly bound to ADP, appears unchanged between the LIS1-bound and unbound dynein (Fig. 6c). Among the exceptions are the following small differences at the LIS1-binding sites (Fig. 6d): the tip of the buttress is shifted 3.1 Å toward the site^{stalk}-bound LIS1, which results in a 1.7-Å shift of CC2 toward CC1 of the stalk; and, the AAA5 loop is shifted 1.4 Å away from the site^{ring}-bound LIS1. The overall conformational similarities between these two dynein structures are consistent with recent findings that LIS1 does not in fact impact dynein’s

mechanochemistry or microtubule-binding behavior². Rather, our findings suggest that dynein’s conformational state impacts its ability to bind LIS1, but not vice versa.

The linker domain is thought to adopt one of two states: a pre-powerstroke state, in which the linker is bent by ~90°, and a post-powerstroke state, in which the linker is straight^{44–46}. Given that ATP and vanadate promote the adoption of the pre-powerstroke state³⁷ and stimulate dynein–LIS1 binding²⁹, it is possible that a straight linker precludes LIS1 binding owing to the close proximity of LIS1 to the amino terminus of the linker, and thus potential steric hinderance²⁷. Although our dynein_{MOTOR}^{MT-B} structure clearly possesses a straight linker (Fig. 5a), the N-terminal region of the linker of both LIS1-bound and LIS1-unbound dynein_{MOTOR}^{MT-U} exhibited pronounced flexibility in spite of the presence of ATP and vanadate. Using 3D classification, we found that this region samples a range of conformations, from bent to straight (Extended Data Fig. 10). These observations suggest that the linker conformation is not necessarily predictive of LIS1 binding.

Changes at the ring site account for reduced LIS1 affinity

Global alignment of MT-U and MT-B reveal the changes initiated by microtubule binding and the consequent CC1–CC2 helix sliding in the stalk⁴⁷. Movement of CC2 with respect to CC1 causes the tip of the buttress to shift away from the AAA+ ring. This leads to a deep kink in the middle of the buttress and a consequent rigid body movement of the AAA5–AAA6L subdomains. This causes the AAA+ ring to adopt a more open state that can no longer coordinate Pi binding at AAA1 (Extended Data Fig. 5h and Supplementary Video 3). We wondered whether these changes, spanning one side of the AAA+ ring (AAA1, AAA5, AAA6), lead to allostery on the other side (that is, at site^{ring} and site^{stalk}) that would influence dynein–LIS1 affinity. Local alignment of MT-U and MT-B using AAA4–AAA5 revealed several notable changes at both LIS1 binding interfaces, including the following: at site^{stalk}, the tip of the buttress is shifted 10.3 Å away from LIS1 (Fig. 7a); at site^{ring}, both the AAA4 helix (residues 2886–2903) and the AAA3 loop (residues 2875–2880) are shifted 4.4–6.5 Å away from the AAA5 loop (residues 3654–3661), thus increasing the spacing between these three elements that all make direct contacts with LIS1 (Figs. 5d and 7b and Supplementary Video 4). This latter change is likely sufficient to weaken LIS1’s binding affinity for site^{ring}.

Our data suggest that LIS1 binding to dynein is initiated at site^{ring}, and is followed by binding at site^{stalk}. This is further supported by the fact that a monomeric Pac1 binds predominantly at site^{ring}, with no apparent binding at site^{stalk} (ref. 27). Thus, we sought to determine whether structural changes at site^{ring} are responsible for the altered Pac1- and LIS1-binding affinity. To this end, we specifically interrogated this site by assessing the binding between dynein and a monomeric Pac1 mutant (lacking its N-terminal dimerization domain; Pac1^{ΔN}). We found that, much like the Pac1 dimer, Pac1^{ΔN} binds dynein_{MOTOR}^{MT-U} to a greater extent than dynein_{MOTOR}^{MT-B} (Fig. 7c). To ensure that Pac1^{ΔN} was

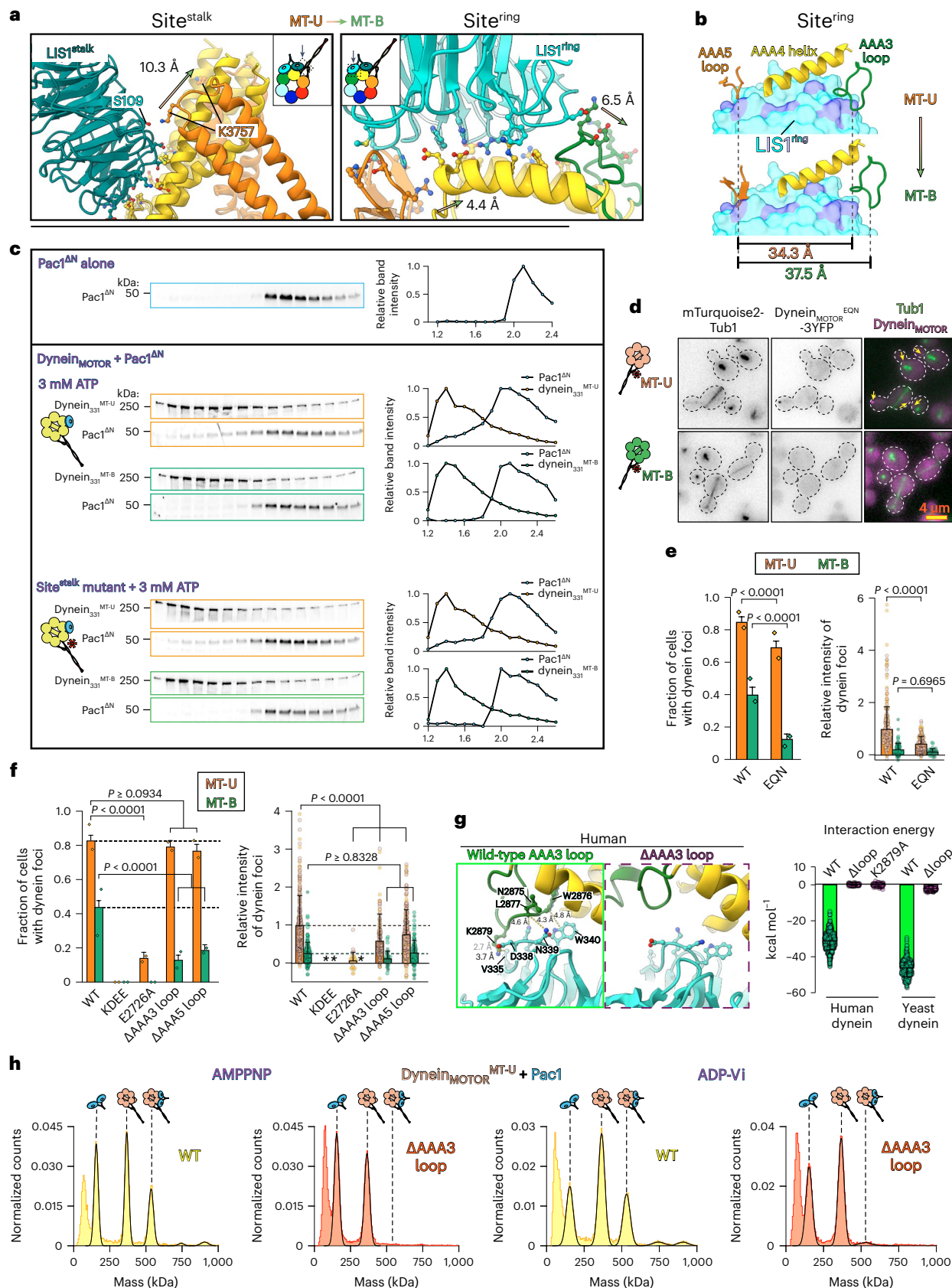
Fig. 7 | Changes at site^{ring} account for reduced LIS1 and Pac1 binding affinity.

a, Close-up views illustrating differences between dynein_{MOTOR}^{MT-U} and dynein_{MOTOR}^{MT-B} at site^{stalk} and site^{ring} (dynein_{MOTOR}^{MT-B} is depicted with reduced opacity compared with dynein_{MOTOR}^{MT-U}). Arrows indicate notable differences. Residues with atoms shown are those determined to mediate contacts between dynein and LIS1. **b**, Summary of major changes at site^{ring}. Purple residues on LIS1 are those that make contact with site^{ring}. **c**, Analytical size-exclusion chromatography analysis of monomeric Pac1^{ΔN} alone or Pac1^{ΔN} mixed with indicated yeast dynein_{MOTOR} before being run on a Superdex 5/150. Plots depict band intensity profiles. Gels and analyses are representative of at least three independent replicates. **d**, Representative images of cells expressing mTurquoise2-Tub1 and dynein_{MOTOR} with EQN substitutions (arrows, plus-end foci). **e,f**, Plots (mean ± s.d., along with all data points) depicting frequency and relative intensity of the indicated dynein foci (for **e**: *n* = 300 foci from 246 dynein_{MOTOR}^{MT-U} cells; 95 foci from 222 dynein_{MOTOR}^{MT-B} cells; 232 foci from 290

dynein_{MOTOR}^{MT-U[EQN]} cells; 33 foci from 220 dynein_{MOTOR}^{MT-B[EQN]} cells; for **f**: *n* = 339 foci from 263 dynein_{MOTOR}^{MT-U} cells; 158 foci from 316 dynein_{MOTOR}^{MT-B} cells; 0 foci from 203 dynein_{MOTOR}^{MT-U[KDEE]} cells; 0 foci from 284 dynein_{MOTOR}^{MT-B[KDEE]} cells; 31 foci from 212 dynein_{MOTOR}^{MT-U[E2726A]} cells; 0 foci from 284 dynein_{MOTOR}^{MT-B[E2726A]} cells; 229 foci from 251 dynein_{MOTOR}^{MT-U[AAA3 loop]} cells; 41 foci from 284 dynein_{MOTOR}^{MT-B[AAA3 loop]} cells; 312 foci from 238 dynein_{MOTOR}^{MT-U[AAA5 loop]} cells; 92 foci from 319 dynein_{MOTOR}^{MT-B[AAA5 loop]} cells; all from 2 biological replicates). **g**, Plot (mean ± s.d., along with all data points) depicting results of MD simulations showing the energy of interaction between wild-type or mutant human or yeast dynein with LIS1 or Pac1, respectively (from left to right, *n* = 1,024, 163, 134, 335, 401 iterations). **h**, Mass photometric analysis of the indicated proteins in the indicated nucleotides. Histograms depict representative data of at least 3 independent replicates each, all of which showed the same results. For **e** and **f**, two-tailed *P* values were calculated from *Z* scores for proportion data, or by comparing means using a Dunnett’s test (for intensity values).

binding to site^{ring}, we repeated this binding assay using dynein variants with three point mutations that interfere with Pac1-site^{stalk} binding: p.E3012A, p.Q3014A, and p.N3018A ('EQN' mutant)⁴⁰. This revealed an identical binding disparity of Pac1^{ΔN} for the MT-U and MT-B mutants

(Fig. 7c, bottom). We validated these findings in cells by assessing the localization of EQN dynein^{MOTOR} MT-U and dynein^{MOTOR} MT-B mutants to microtubule plus-ends. Although both exhibited reduced plus-end localization with respect to the wild-type versions, the two proteins



exhibited localization disparities similar to that of the wild-type MT-U and MT-B fragments (Fig. 7d,e). These data are consistent with a role for site^{stalk} in dynein–Pac1 binding, and indicate that site^{ring} indeed undergoes a conformational change that weakens its affinity for Pac1 and LIS1 upon microtubule binding.

We next focused on the structural elements at site^{ring} that may account for the microtubule-binding-induced Pac1 and LIS1 dissociation: the AAA4 helix, the AAA3 loop, and the AAA5 loop, which move with respect to each other upon microtubule binding (Fig. 7a,b and Supplementary Video 4). Consistent with the importance of the AAA4 helix in dynein–Pac1 binding, mutating either four residues (p.K2721A, p.D2725G, p.E2726S, and p.E2727G; ‘KDEE’ mutant²⁸) or only one (p.E2726A; equivalent to E2903 in human dynein) severely reduces plus-end binding of both dynein_{MOTOR}^{MT-U} and dynein_{MOTOR}^{MT-B} in cells (Fig. 7f). Furthermore, deleting two key residues in the AAA5 loop³⁹ (N3475 and R3476) significantly reduces plus-end binding by MT-U and MT-B (Fig. 7f), consistent with the importance of this surface in Pac1 binding³⁹. We next focused on the AAA3 loop as a potential Pac1- and LIS1-binding surface that changes in response to microtubule binding. In support of the importance of this interface, which includes a salt bridge between LIS1 D388 and dynein K2879, MD simulation data reveal that the cancer-correlated D388G substitution in LIS1 significantly reduces binding energy (Fig. 5e–g and Extended Data Fig. 6d). Additional MD simulations reveal that deleting this loop (Δ2875–2880) or mutating K2879 to an alanine in human dynein, or deleting this loop in yeast dynein (Δ2678–2703), reduces binding energy between dynein and LIS1 and Pac1 (Fig. 7g). Yeast cells expressing dynein_{MOTOR}^{MT-U}-3YFP or dynein_{MOTOR}^{MT-B}-3YFP mutants with this loop deleted (Δ2698–2703) exhibit significant reductions in foci intensity (Fig. 7f). Finally, mass photometric analysis revealed that deletion of the AAA3 loop severely reduces binding of Pac1 to dynein_{MOTOR}^{MT-U}, in spite of the presence of AMPPNP or ATP and Vi (Fig. 7h). These data demonstrate the importance of this loop in the dynein–LIS1 and dynein–Pac1 interaction, and indicate that the conformational changes at site^{ring} that result from microtubule binding likely account for disruption of the dynein–LIS1 complex.

Discussion

Our work reveals insights into the final step of the LIS1-mediated dynein activation pathway. Our findings strongly suggest that microtubule binding by dynein triggers its dissociation from LIS1, and that this is required to uncouple the dynein transport complex from the plus-end-targeting machinery (for example, Bik1/CLIP-170 in yeast, and EB1 in metazoa)^{17,18,20,48}. This dissociation is required for dynein to switch from a plus-end-bound state, in which it is only indirectly associated with the microtubule, to a motile state, in which it is directly engaged with the microtubule lattice. Dynein is in a microtubule-unbound conformation when it is at the plus end. Preventing its switching to a microtubule-bound state locks dynein in this plus-end-associated state in cells. In light of the similar affinity of wild-type and dynein_{MOTOR}^{MT-U} for Pac1 and LIS1 in vitro, it is the microtubule-bound state that is a unique conformational state that exhibits low affinity for Pac1 and LIS1. In addition to revealing the structural basis for the weakened affinity, we find that LIS1 binding to dynein is governed by the conformational state of dynein, but that LIS1 binding has very little effect on dynein's conformation, at least in the context of our ADP-Vi-bound MT-U mutant.

We posit the following model for Pac1 function in budding yeast (see Supplementary Video 5): (1) dynein stochastically switches between phi and open states in the cytoplasm^{2,3}; (2) once in an open state, Pac1 binds to dynein owing to the increased accessibility of Pac1-binding surfaces, thus preventing dynein from switching back to the phi particle^{2,10}; (3) dynein–Pac1 binds to plus-end-bound Bik1 (ref. 21); (4) dynactin associates with plus-end-bound dynein; (5) dynein–dynactin binds to cortical Num1, which triggers dynein–microtubule binding, potentially by arranging the motor domains in a parallel configuration³; (6) microtubule binding by dynein

triggers conformational changes that include a distortion of site^{ring} that weakens its affinity for Pac1; (7) Pac1 dissociates from dynein, thus breaking dynein's indirect connection to the plus-end; (8) dynein–dynactin directly engages with the microtubule, and translocates the mitotic spindle. In light of the similarities between the yeast and metazoan systems⁷, and our data from human dynein and LIS1, we posit that a very similar mechanism is at play in animal cells.

Given that dynein is in a microtubule-unbound conformation at plus-ends, and that the dynein MTBD is dispensable for this association²¹, our work indicates that Pac1 (and likely LIS1) does not in fact promote plus-end binding by impacting dynein's microtubule-binding behavior. In fact, we show that once dynein makes direct contact with the microtubule, this leads to a consequent dissociation of dynein from Pac1. This likely explains the lack of Pac1- and LIS1-dynein colocalization at sites of dynein activity^{22–24}. These data are further supported by our cryo-EM structures for dynein_{MOTOR}^{MT-U} in the absence and presence of LIS1, which show very little differences between them.

Our work also reveals a high-resolution structure of a human dynein–LIS1 complex that highlights precise residues that link these molecules together. Our 3D classification analysis of the different LIS1-bound dynein species reveal insight into the importance of the site^{stalk}-bound LIS1 and support an avidity model in which two binding sites on dynein improves LIS1 binding. This is consistent with data indicating that a Pac1 monomer in yeast can rescue function only if it is overexpressed²⁸. The importance of LIS1–LIS1 binding is further highlighted by the presence of disease-correlated missense mutations in the LIS1 LisH dimerization domain (for example, p.F31S, p.L43S, p.W55M)^{49–51}.

Although our work reveals the likely basis for dynein–Pac1 and dynein–LIS1 dissociation, we cannot completely discount other changes that might contribute to this process. For example, a previous study has found that the N-terminal region of the dynein linker element encounters Pac1 during its powerstroke²⁷. One potential hypothesis is that the linker swing may thus partly account for the dissociation (that is, by knocking it off). However, in contrast to this possibility, we have found that dynein with a shortened linker that does not encounter Pac1 (ref. 27) is sufficient for dissociation. This is further supported by our 3D classification analysis, which revealed that a straight linker is not necessarily incompatible with LIS1 binding. Finally, given the apparent contact between the tip of the buttress of dynein_{MOTOR}^{MT-U} and the site^{stalk}-bound LIS1, the affinity of LIS1 for site^{stalk} is likely also weakened by microtubule binding.

Online content

Any methods, additional references, Nature Portfolio reporting summaries, source data, extended data, supplementary information, acknowledgements, peer review information; details of author contributions and competing interests; and statements of data and code availability are available at <https://doi.org/10.1038/s41594-023-01010-x>.

References

- Canty, J. T., Tan, R., Kusakci, E., Fernandes, J. & Yildiz, A. Structure and mechanics of dynein motors. *Annu. Rev. Biophys.* **50**, 549–574 (2021).
- Marzo, M. G., Griswold, J. M. & Markus, S. M. Pac1/LIS1 stabilizes an uninhibited conformation of dynein to coordinate its localization and activity. *Nat. Cell Biol.* **22**, 559–569 (2020).
- Zhang, K. et al. Cryo-EM reveals how human cytoplasmic dynein is auto-inhibited and activated. *Cell* **169**, 1303–1314 (2017).
- Amos, L. A. Brain dynein crossbridges microtubules into bundles. *J. Cell Sci.* **93**, 19–28 (1989).
- McKenney, R. J., Huynh, W., Tanenbaum, M. E., Bhabha, G. & Vale, R. D. Activation of cytoplasmic dynein motility by dynactin–cargo adapter complexes. *Science* **345**, 337–341 (2014).

6. Schlager, M. A., Hoang, H. T., Urnavicius, L., Bullock, S. L. & Carter, A. P. In vitro reconstitution of a highly processive recombinant human dynein complex. *EMBO J.* **33**, 1855–1868 (2014).
7. Markus, S. M., Marzo, M. G. & McKenney, R. J. New insights into the mechanism of dynein motor regulation by lissencephaly-1. *eLife* **9**, e59737 (2020).
8. Reiner, O. et al. Isolation of a Miller–Dieker lissencephaly gene containing G protein beta-subunit-like repeats. *Nature* **364**, 717–721 (1993).
9. Qiu, R., Zhang, J. & Xiang, X. LIS1 regulates cargo-adaptor-mediated activation of dynein by overcoming its autoinhibition in vivo. *J. Cell Biol.* **218**, 3630–3646 (2019).
10. Htet, Z. M. et al. LIS1 promotes the formation of activated cytoplasmic dynein-1 complexes. *Nat. Cell Biol.* **22**, 518–525 (2020).
11. Elshenawy, M. M. et al. Lis1 activates dynein motility by modulating its pairing with dynactin. *Nat. Cell Biol.* **22**, 570–578 (2020).
12. Lee, W. L., Oberle, J. R. & Cooper, J. A. The role of the lissencephaly protein Pac1 during nuclear migration in budding yeast. *J. Cell Biol.* **160**, 355–364 (2003).
13. Coquelle, F. M. et al. LIS1, CLIP-170's key to the dynein/dynactin pathway. *Mol. Cell Biol.* **22**, 3089–3102 (2002).
14. Faulkner, N. E. et al. A role for the lissencephaly gene LIS1 in mitosis and cytoplasmic dynein function. *Nat. Cell Biol.* **2**, 784–791 (2000).
15. Moon, H. M. et al. LIS1 controls mitosis and mitotic spindle organization via the LIS1–NDEL1–dynein complex. *Hum. Mol. Genet.* **23**, 449–466 (2014).
16. Splinter, D. et al. BICD2, dynactin, and LIS1 cooperate in regulating dynein recruitment to cellular structures. *Mol. Biol. Cell* **23**, 4226–4241 (2012).
17. Sheeman, B. et al. Determinants of *S. cerevisiae* dynein localization and activation: implications for the mechanism of spindle positioning. *Curr. Biol.* **13**, 364–372 (2003).
18. Baumbach, J. et al. Lissencephaly-1 is a context-dependent regulator of the human dynein complex. *eLife* **6**, e21768 (2017).
19. Gutierrez, P. A., Ackermann, B. E., Vershinin, M. & McKenney, R. J. Differential effects of the dynein-regulatory factor Lissencephaly-1 on processive dynein-dynactin motility. *J. Biol. Chem.* **292**, 12245–12255 (2017).
20. Jha, R., Roostalu, J., Cade, N. I., Trokter, M. & Surrey, T. Combinatorial regulation of the balance between dynein microtubule end accumulation and initiation of directed motility. *EMBO J.* **36**, 3387–3404 (2017).
21. Lammers, L. G. & Markus, S. M. The dynein cortical anchor Num1 activates dynein motility by relieving Pac1/LIS1-mediated inhibition. *J. Cell Biol.* **211**, 309–322 (2015).
22. Lenz, J. H., Schuchardt, I., Straube, A. & Steinberg, G. A dynein loading zone for retrograde endosome motility at microtubule plus-ends. *EMBO J.* **25**, 2275–2286 (2006).
23. Egan, M. J., Tan, K. & Reck-Peterson, S. L. Lis1 is an initiation factor for dynein-driven organelle transport. *J. Cell Biol.* **197**, 971–982 (2012).
24. Markus, S. M. & Lee, W. L. Regulated offloading of cytoplasmic dynein from microtubule plus ends to the cortex. *Dev. Cell* **20**, 639–651 (2011).
25. Markus, S. M. et al. Quantitative analysis of Pac1/LIS1-mediated dynein targeting: Implications for regulation of dynein activity in budding yeast. *Cytoskeleton* **68**, 157–174 (2011).
26. Hu, C. D., Chinenov, Y. & Kerppola, T. K. Visualization of interactions among bZIP and Rel family proteins in living cells using bimolecular fluorescence complementation. *Mol. Cell* **9**, 789–798 (2002).
27. Toropova, K. et al. Lis1 regulates dynein by sterically blocking its mechanochemical cycle. *eLife* **3**, e03372 (2014).
28. Huang, J., Roberts, A. J., Leschziner, A. E. & Reck-Peterson, S. L. Lis1 acts as a 'clutch' between the ATPase and microtubule-binding domains of the dynein motor. *Cell* **150**, 975–986 (2012).
29. McKenney, R. J., Vershinin, M., Kunwar, A., Vallee, R. B. & Gross, S. P. LIS1 and NudE induce a persistent dynein force-producing state. *Cell* **141**, 304–314 (2010).
30. Lacey, S. E., He, S., Scheres, S. H. & Carter, A. P. Cryo-EM of dynein microtubule-binding domains shows how an axonemal dynein distorts the microtubule. *eLife* **8**, e47145 (2019).
31. Nishida, N. et al. Structural basis for two-way communication between dynein and microtubules. *Nat. Commun.* **11**, 1038 (2020).
32. Carter, A. P. et al. Structure and functional role of dynein's microtubule-binding domain. *Science* **322**, 1691–1695 (2008).
33. Gibbons, I. R. et al. The affinity of the dynein microtubule-binding domain is modulated by the conformation of its coiled-coil stalk. *J. Biol. Chem.* **280**, 23960–23965 (2005).
34. Kon, T. et al. Helix sliding in the stalk coiled coil of dynein couples ATPase and microtubule binding. *Nat. Struct. Mol. Biol.* **16**, 325–333 (2009).
35. Markus, S. M., Punch, J. J. & Lee, W. L. Motor- and tail-dependent targeting of dynein to microtubule plus ends and the cell cortex. *Curr. Biol.* **19**, 196–205 (2009).
36. Young, G. et al. Quantitative mass imaging of single biological macromolecules. *Science* **360**, 423–427 (2018).
37. Schmidt, H., Zalyte, R., Urnavicius, L. & Carter, A. P. Structure of human cytoplasmic dynein-2 primed for its power stroke. *Nature* **518**, 435–438 (2015).
38. Chaaban, S. & Carter, A. P. Structure of dynein-dynactin on microtubules shows tandem adaptor binding. *Nature* **610**, 212–216 (2022).
39. Gillies, J. P. et al. Structural basis for cytoplasmic dynein-1 regulation by Lis1. *eLife* **11**, e71229 (2022).
40. DeSantis, M. E. et al. Lis1 has two opposing modes of regulating cytoplasmic dynein. *Cell* **170**, 1197–1208 (2017).
41. Reimer, J. M., DeSantis, M. E., Reck-Peterson, S. L. & Leschziner, A. E. Structures of human dynein in complex with the lissencephaly 1 protein, LIS1. *eLife* **12**, e84302 (2023).
42. Torres, F. R. et al. Mutation screening in a cohort of patients with lissencephaly and subcortical band heterotopia. *Neurology* **62**, 799–802 (2004).
43. Tate, J. G. et al. COSMIC: the Catalogue Of Somatic Mutations In Cancer. *Nucleic Acids Res.* **47**, D941–D947 (2019).
44. Burgess, S. A., Walker, M. L., Sakakibara, H., Knight, P. J. & Oiwa, K. Dynein structure and power stroke. *Nature* **421**, 715–718 (2003).
45. Kon, T., Nishiura, M., Ohkura, R., Toyoshima, Y. Y. & Sutoh, K. Distinct functions of nucleotide-binding/hydrolysis sites in the four AAA modules of cytoplasmic dynein. *Biochemistry* **43**, 11266–11274 (2004).
46. Imamula, K., Kon, T., Ohkura, R. & Sutoh, K. The coordination of cyclic microtubule association/dissociation and tail swing of cytoplasmic dynein. *Proc. Natl Acad. Sci. USA* **104**, 16134–16139 (2007).
47. Uchimura, S. et al. A flipped ion pair at the dynein-microtubule interface is critical for dynein motility and ATPase activation. *J. Cell Biol.* **208**, 211–222 (2015).
48. Duellberg, C. et al. Reconstitution of a hierarchical +TIP interaction network controlling microtubule end tracking of dynein. *Nat. Cell Biol.* **16**, 804–811 (2014).
49. Cardoso, C. et al. The location and type of mutation predict malformation severity in isolated lissencephaly caused by abnormalities within the LIS1 gene. *Hum. Mol. Genet.* **9**, 3019–3028 (2000).

50. Pilz, D. T. et al. LIS1 and XLIS (DCX) mutations cause most classical lissencephaly, but different patterns of malformation. *Hum. Mol. Genet.* **7**, 2029–2037 (1998).
51. Sapir, T. et al. Analysis of lissencephaly-causing LIS1 mutations. *Eur. J. Biochem.* **266**, 1011–1020 (1999).

Publisher's note Springer Nature remains neutral with regard to jurisdictional claims in published maps and institutional affiliations.

Springer Nature or its licensor (e.g. a society or other partner) holds exclusive rights to this article under a publishing agreement with the author(s) or other rightsholder(s); author self-archiving of the accepted manuscript version of this article is solely governed by the terms of such publishing agreement and applicable law.

© The Author(s), under exclusive licence to Springer Nature America, Inc. 2023

Methods

Media and strain construction

Strains were derived from either W303 (for protein purification) or YEF473 (for cell imaging)⁵². We transformed yeast strains using the lithium acetate method⁵³. Strains carrying substitutions, insertions (for example, SRS^{CC}), or tagged components were constructed by PCR product-mediated transformation⁵⁴, by transforming plasmids with recombination or expression cassettes^{2,35}, or by mating followed by tetrad dissection. Proper tagging and mutagenesis was confirmed by PCR, and in most cases sequencing. Fluorescent tubulin-expressing yeast strains were generated using plasmids and strategies described previously⁵⁵. Yeast synthetic defined (SD) medium was obtained from Sunrise Science Products.

Plasmid and BACmid construction

To construct yeast strains expressing SRS^{CC}-containing yeast dynein motor domain fragments (dynein_{MOTOR}^{MT-U} and dynein_{MOTOR}^{MT-B}), we used PCR-product mediated engineering or plasmid-based recombination with various engineered pSM01:Dyn1_{MOTOR}-3YFP plasmids (generated using Gibson assembly^{35,56}; see Supplementary Table 2 for primers used). The seryl tRNA synthetase coiled-coil (residue 30–96) was amplified from *T. thermophilus* (strain BB8) genomic DNA and integrated into the native *DYN1* locus in yeast to achieve the sequences depicted in Extended Data Fig. 1b (note the presence of four additional amino acids in the MT-B mutant with respect to MT-U). The pSM01:Dyn1_{MOTOR}-3YFP plasmids were generated by amplifying the engineered region from the resulting yeast strains, and all subsequent mutants were engineered into this plasmid (for example, EQN, KDEE), which was digested (with BsaBI/BsiWI; to release the respective dynein open reading frame along with a *TRP1* marker, all of which is flanked with homology arms) and subsequently transformed into *dyn1Δ::HIS3* yeast. The entire cassette was integrated into the *DYN1* locus (resulting in HIS⁺ TRP⁺ cells), and was the only source of dynein in these cells. Genomic integration was confirmed by growth on selective solid medium (one lacking histidine, and another lacking tryptophan), and by PCR.

The human dynein motor domain (residues 1458–4646) was amplified from pbiG1a:6XHis-ZZ-TEV-SNAPf-DHC (codon optimized for insect cells; a gift from A. Carter)⁵⁷ and assembled into pFastBac:8His-ZZ-TEV-LIS1-SNAPf (replacing LIS1-SNAPf), generating pFastBac:8His-ZZ-TEV-DHC_{MOTOR}. The SRS^{CC} from *T. thermophilus* was engineered into this plasmid to generate the MT-U and MT-B mutants. These plasmids (along with pFastBac:8His-ZZ-TEV-LIS1-SNAPf) were individually transformed into DH10 EMBacY cells (Geneva Biotech), according to the manufacturer's protocol. Proper transposition and BACmid generation was confirmed by blue/white screening, and by PCR.

Protein purification

Purification of yeast dynein (wild-type and mutants; ZZ-TEV-dynein₃₃₁-HALO, or ZZ-TEV-6His-GFP-3HA-GST-dynein₃₃₁-HALO, all under the control of the galactose-inducible promoter, *GAL1p*) or Pac1-SNAP was performed as previously described^{2,28,58}. Briefly, yeast cultures were grown in YPA supplemented with 2% galactose, collected, washed with cold water, and then resuspended in a small volume of water. The resuspended cell pellet was drop frozen into liquid nitrogen and then lysed in a coffee grinder (Hamilton Beach). After lysis, 0.25 volume of 4× lysis buffer (1× buffer: 30 mM HEPES, pH 7.2, 50 mM potassium acetate, 2 mM magnesium acetate, 0.2 mM EGTA) supplemented with 1 mM DTT, 0.1 mM Mg-ATP, 0.5 mM Pefabloc SC (concentrations for 1× buffer) was added, and the lysate was clarified at 310,000g for 1 hour. The supernatant was then bound to IgG sepharose 6 fast flow resin (Cytiva) for 2–4 h at 4 °C, which was subsequently washed three times in 5 ml lysis buffer and twice in TEV buffer (50 mM Tris, pH 8.0, 150 mM potassium acetate, 2 mM magnesium acetate, 1 mM EGTA, 0.005% Triton X-100, 10% glycerol, 1 mM DTT, 0.1 mM Mg-ATP, 0.5 mM Pefabloc SC). To fluorescently label the proteins, the bead-bound protein

was incubated with either 10 μM JFX646-HaloTag (for the motors) or JF646-SNAP-tag ligand (for Pac1; Janelia Research Campus) for 30–60 min at 4 °C. The resin was then washed four more times in TEV buffer, then incubated in TEV buffer supplemented with TEV protease overnight at 4 °C. Following TEV digest, the protein-containing supernatant was collected using a spin filtration device, aliquoted, flash frozen in liquid nitrogen, and stored at –80 °C.

Human proteins (LIS1-SNAP, or motor domains) were expressed and purified from insect cells (ExpiSf9 cells; Life Technologies) as previously described, with minor modifications^{3,6,18,57}. Briefly, 4 ml of ExpiSf9 cells at 2.5×10^6 cells ml⁻¹, which were maintained in ExpiSf CD Medium (Life Technologies), were transfected with 1–9 μg of bacmid DNA using ExpiFectamine (Life Technologies), according to the manufacturer's instructions. At 4–8 d after transfection, the cells were pelleted, and 1–2 ml of the resulting supernatant (P1) was used to infect ~150 ml of ExpiSf9 cells (5×10^6 cells ml⁻¹). Approximately 65 h later, the cells were collected (2,000g, 20 min), washed with human dynein lysis buffer (50 mM HEPES, pH 7.4, 100 mM NaCl, 10% glycerol, 1 mM DTT, 0.1 mM Mg-ATP, 1 mM PMSF; ATP was omitted for LIS1 purification), pelleted again (1,810g, 20 min), and resuspended in an equal volume of the same buffer. The resulting cell suspension was drop frozen in liquid nitrogen and stored at –80 °C. For protein purification, 30 ml of additional human dynein lysis buffer supplemented with cOMplete protease inhibitor cocktail (Roche) was added to the frozen cell pellet, which was then rapidly thawed in a 37 °C water bath prior to incubation on ice. Cells were lysed in a dounce-type tissue grinder (Wheaton) using 50–60 strokes. After clarification at 310,000g for 1 h, the supernatant was applied to 2 ml of IgG sepharose fast flow resin (GE) pre-equilibrated in human dynein lysis buffer, and incubated at 4 °C for 3–5 h. Beads were then washed 3 times with 5–10 ml of human dynein lysis buffer, and 2 times with 5–10 ml of human dynein TEV buffer (50 mM Tris pH 7.4, 150 mM potassium acetate, 2 mM magnesium acetate, 1 mM EGTA, 10% glycerol, 1 mM DTT, 0.1 mM Mg-ATP; note ATP was omitted for LIS1 purification). The beads were incubated with TEV protease overnight at 4 °C. The next morning, the recovered supernatant was collected, concentrated, aliquoted, flash frozen, and stored at –80 °C. Protein used for cryo-EM was processed directly without freezing. LIS1-SNAP required a gel filtration step to improve purity for mass photometry. To this end, the TEV eluate was injected on to a Superdex 200 10/300 equilibrated in TEV buffer (without ATP). Peak fractions were pooled, concentrated, aliquoted, snap frozen and stored at –80 °C.

Dynein ATPase assays

ATPase activities were determined using the EnzChek phosphate assay kit (Life Technologies). Assays were performed in motility buffer (30 mM HEPES pH 7.2, 50 mM potassium acetate, 2 mM magnesium acetate, 1 mM EGTA, 1 mM DTT) supplemented with 2 mM MgATP, with or without 2 μM taxol-stabilized microtubules. Reactions were initiated with the addition of 5 nM 6xHis-GST-dynein₃₃₁ (wild-type or mutants), and the absorbance at 360 nm was monitored by a spectrophotometer for 10–20 min. Background phosphate release levels (presumably from microtubules) for each reaction were measured for 5 min before addition of dynein to account for any variation as a consequence of differing microtubule concentrations, and were subtracted from each data point.

Dynein microtubule-binding assays

Flow chambers constructed using slides and plasma-cleaned and silanized coverslips, attached with double-sided adhesive tape, were coated with anti-tubulin antibody (8 μg ml⁻¹, YL1/2; Accurate Chemical & Scientific Corporation), then blocked with a mixture of 1% Pluronic F-127 (Thermo Fisher Scientific) and 1 mg ml⁻¹ κ-casein. Taxol-stabilized microtubules assembled from porcine tubulin (Cytoskeleton) were introduced into the chamber. After microtubules adhered to the cover glass, 50 nM dynein_{MOTOR} fragments (wild-type or mutant) diluted in TEV buffer was flowed into the chambers. After a brief incubation

(2–5 min), images were acquired at room temperature using a 1.49-NA $\times 100$ objective on a total internal reflection fluorescence (TIRF) Ti-E inverted microscope (Nikon), equipped with a SOLA SM II LE LED light engine (Lumencor), a motorized filter cube turret, and an iXon X3 DU897 cooled EM-CCD camera (Andor). A 640-nm laser (Nikon) was used along with a multi-pass quad filter cube set (C-TIRF for 405/488/561/638 nm; Chroma) and an emission filter mounted in a filter wheel (700/75 nm; Chroma) to image dynein_{MOTOR}-HaloTag^{JFX646}.

Live cell imaging experiments

Cells were grown to mid-log phase in SD medium supplemented with 2% glucose, and mounted on agarose pads. Images were collected at room temperature using a 1.49 NA $\times 100$ objective on a Ti-E inverted microscope equipped with a Ti-S-E motorized stage (Nikon), piezo Z-control (Physik Instrumente), a SOLA SM II LE LED light engine (Lumencor), a motorized filter cube turret, and an iXon X3 DU897 cooled EM-CCD camera (Andor). The microscope system was controlled by NIS-Elements software (Nikon). Step sizes of 0.5 μm (for Bik1-3mCherry quantitation) or 1 μm (for dynein quantification) were used to acquire 2- μm -thick Z-stack images. Sputtered/ET filter cube sets (Chroma Technology) were used for imaging mTurquoise2 (49001), GFP (49002), YFP (49003), and mCherry (49008) fluorescence. Images were analyzed using FIJI/ImageJ. Plus-end and cortical foci were scored (frequency and intensity) from maximum-intensity projected time-lapse movies. All foci were scored from time-lapse movies. Those foci observed moving coincident with the ends of microtubules were scored as plus-end-associated, while those that appeared to be statically associated with the cortex for ≥ 3 frames were scored as cortically associated. Intensity values plotted throughout are background corrected as follows: a 3×3 box drawn around each focus was used to measure signal, while the same size box was drawn around an adjacent region in the cytoplasm to measure background, which was subtracted from the signal. For Figure 1, all dynein and Pac1 intensity values were normalized to the mean values (for each replicate) of plus-end-associated dynein and Pac1, respectively, in wild-type cells (each set to 1). For Figure 7e,f, all intensity values were normalized to the mean values (for each replicate) for dynein_{MOTOR}^{MT-U}-3YFP (set to 1).

Analytical size-exclusion chromatography

To assess dynein_{MOTOR}-Pac1 binding, equal concentrations of purified motor proteins ($\sim 8 \mu\text{g}$ dynein_{MOTOR}-HaloTag^{JFX646}) were first incubated in the indicated nucleotide (3 mM each) for 10 min on ice, followed by addition of Pac1-SNAP^{JFX646} ($\sim 2 \mu\text{g}$; final concentrations of each were between 400–600 nM each). Following a 10-min incubation on ice, the mixture was injected on to a Superdex 5/150 using an AKTA Pure. Fractions with JFX646-labeled proteins were separated by SDS-PAGE, which were subsequently scanned using a Typhoon gel imaging system (FLA 9500). FIJI was used to determine background-subtracted band intensity.

Mass photometry

With the exception of LIS1-SNAP, all purified proteins were used directly for mass photometry, without additional purification steps. LIS1-SNAP required an additional gel filtration step to remove higher-molecular-weight species (as determined by mass photometry; see above). All proteins were initially diluted to 500 nM in assay buffer (50 mM Tris, pH 8.0, 150 mM potassium acetate, 2 mM magnesium acetate, 1 mM EGTA, 1 mM DTT) with or without added nucleotide (1 mM of each, as indicated in figures), and then were subsequently diluted to 50 nM in the same buffer. Three microliters of each protein was then mixed 1:1 (to 25 nM of each), incubated for 1–2 min, and then diluted 1:5 on the stage (2.5 μl of mixed protein + 10 μl same buffer with or without nucleotide) to 5 nM final immediately before image acquisition. For apo conditions, residual ATP from the protein preparation was depleted using apyrase by mixing 4.5 μl of 500 nM protein with a 0.5 μl of apyrase (NEB) and incubating the mixture for 30 min at room

temperature. One-minute videos were acquired using Refeyn MP, and all images were processed and analyzed using Discover MP. Calibration was performed with β -amylase and thyroglobulin.

Cryo-EM grid preparation

Purified proteins (as described above) were applied to a TSKgel G4000SWXL column pre-equilibrated with 50 mM Tris pH 7.4, 150 mM potassium acetate, 2 mM magnesium acetate, 1 mM EGTA, 1 mM DTT, and 0.1 mM Mg-ATP. Peak fractions were pooled and 1 mM Mg-ATP with (for MT-U proteins) or without (for MT-B) 1 mM Na_3VO_4 was immediately added. Protein quality was examined by negative staining microscopy. Glycerol was added to a final concentration of 10%, aliquots were flash-frozen in liquid nitrogen and stored at -80°C . For initial cryo-EM analysis of the human dynein MT-B mutant in ATP buffer (50 mM Tris pH 7.4, 150 mM potassium acetate, 2 mM magnesium acetate, 1 mM EGTA, 1 mM DTT, 1 mM Mg-ATP), we found that a high concentration ($>5 \text{ mg ml}^{-1}$) of protein was required for the protein to enter the open holes of a plasma-cleaned QUANTIFOIL Au R2/1300-mesh grids (Extended Data Fig. 4a). To reduce the sample concentration during cryo-EM grid preparation for human dynein MT-U mutant in buffer supplemented with ATP and Vi (50 mM Tris pH 7.4, 150 mM potassium acetate, 2 mM magnesium acetate, 1 mM EGTA, 1 mM DTT, 1 mM Mg-ATP and 1 mM Na_3VO_4), we coated QUANTIFOIL Cu R2/1300-mesh grids with graphene-oxide (GO) layers, as previously reported⁵⁹. Four microliters of the MT-U mutant with or without human LIS1 at 0.2–0.4 mg ml^{-1} were applied to the graphene-oxide-coated side of freshly prepared GO-grids (Extended Data Fig. 4f,k), followed by a 4-s wait time, 3- to 6-s blot time, 4 blot force, and subsequent freezing in liquid ethane using a Vitrobot Mark IV unit (FEI). The Vitrobot chamber was maintained at close to 95% humidity at 4°C .

Data from MT-B or MT-U alone were collected at the Yale ScienceHill-Cryo-EM facility using a Glacios microscope (Thermo Fisher Scientific), operated at 200 keV. The images were collected with a K2 direct electron detector (Gatan) operating in super-resolution mode, at a nominal magnification of $\times 36,000$, corresponding to a pixel size of 1.149 \AA . Data collection was automated by SerialEM software⁶⁰ with a defocus range of $-1.5 \mu\text{m}$ to $-2.7 \mu\text{m}$. In total, 3,035 movies for MT-B and 3,065 movies for MT-U were collected, and each movie was dose-fractionated to 40 frames with a total dose of $40 \text{ e}^-/\text{\AA}^2$ (Extended Data Fig. 4 and Table 1).

The MT-U + LIS1 data was collected at the Laboratory for BioMolecular Structure (LBMS) using a Titan Krios microscope (Thermo Fisher Scientific) operated at 300 keV and equipped with a K3 detector and a BioQuantum energy filter (Gatan) with a slit width of 15 eV. Data collection was automated by EPU software, with a defocus range of $-1.5 \mu\text{m}$ to $-2.7 \mu\text{m}$, and all videos were recorded in a super-resolution mode at a nominal magnification of $\times 105,000$, corresponding to a pixel size of 0.825 \AA . Each video was dose-fractionated to 50 frames, with a total dose of $50 \text{ e}^-/\text{\AA}^2$. A total of 5,183 videos were collected (Extended Data Fig. 4 and Table 1).

Cryo-EM image processing

Cryo-EM data processing workflows are outlined in Extended Data Fig. 4. Recorded movies were pre-processed using cryoSPARC Live⁶¹, including patch motion correction and patch CTF estimation. Exposures were manually curated, and micrographs without graphene oxide were removed.

For the MT-B dataset (Extended Data Fig. 4a–e), Topaz picker⁶² was used for particle picking. In total, 250,463 particles were extracted, with a box size of 360 with a pixel size of 1.149 \AA . Multiple rounds of 2D classification were performed to filter the particles. Good particles were used for ab initio reconstruction in cryoSPARC. The reconstructed volume was used for several rounds of heterogeneous refinement, followed by 2D classification. Finally, 44,752 particles were selected and subjected to non-uniform refinement⁶³, followed by two rounds of

global and local CTF refinement. A 3.4-Å map was obtained as evaluated using a GSFSC criterion of 0.143.

For the MT-U + LIS1 dataset (Extended Data Fig. 4f–j), Blob picker in cryoSPARC was used for particle picking. An initial 1,400,918 particles were extracted with a box size 500 and were binned to 360 box size, resulting in a pixel size of 1.149 Å. The MT-B map was low-passed to 30 Å and used for heterogeneous refinement. After several rounds of heterogeneous refinement followed by 2D classification, 182,694 particles were selected and subjected to non-uniform refinement. While the dynein motor region was resolved at better resolution, the LIS1 density appeared to be smeared, suggesting flexibility for LIS1 binding. Before performing 3D classification focusing on LIS1 density, we used a mask around the motor region to perform two rounds of global, local CTF refinement, followed by local refinement to better estimate high-order CTF terms and each particle's local defocus value. This yielded a 2.8-Å map of the motor region. We then used a mask around the AAA3-AAA5-2 LIS1 density for local 3D classification without alignment in cryoSPARC. After classification, 3 major classes were obtained: 1 LIS1 bound (66,212 particles, 36.2%), '1.5' LIS1 bound (62,910 particles, 34.4%), and 2 LIS1 bound (53,572 particles, 29.3%; see Extended Data Fig. 9). The 2 LIS1 bound class was subjected to global refinement (motor with 2 LIS1) and local refinement (AAA3-AAA5 with 2 LIS1), yielding a 3.2-Å and 3.3-Å map, respectively.

For the MT-U alone dataset (Extended Data Fig. 4k–o), a similar strategy was used: 729,028 particles picked by the Blob picker were extracted with a box size of 360. Multiple rounds of heterogeneous and 2D classification were used to clean the particles. Finally, 201,717 particles were subjected to non-uniform refinement. Two rounds of global and local CTF refinement followed by local refinement allowed us to obtain a 2.9-Å map.

Local resolution estimation of all maps was performed in cryoSPARC. Directional anisotropy analysis of all maps was performed using 3DFSC⁶⁴, implemented in cryoSPARC.

Model building and refinement

A previously reported human dynein motor structure³ (PDB: 5NUG) was used as an initial model. Individual domains (linker, AAA large, AAA small) were docked into the cryo-EM map as rigid bodies using UCSF ChimeraX⁶⁵. After docking, Namdinator⁶⁶, a MD flexible fitting tool, was used to further fit the model into the cryo-EM map. The model was then manually inspected and adjusted in COOT v0.9.5 (refs. 67,68). The high-resolution cryo-EM map together with our biochemical assay allowed us to confidently assign nucleotides to each pocket. For example, by adjusting the contour level, we could see the separation of vanadate, Mg²⁺, and ADP in the MT-U AAA1 pocket. Our vanadate-mediated photocleavage assay also indicated that vanadate binds to the MT-U AAA1 pocket. These two pieces of evidence allowed us to confidently build ADP-Vi into the MT-U AAA1 pocket.

To build the model for human LIS1, the predicted structure from the AlphaFold⁶⁹ database (AF-P43034) was used as the initial model. The positions of the two LIS1s were determined using a previously reported yeast dynein–Pac1 structure³⁹ (PDB: 7MGM). All models were iteratively refined using Phenix real-space refinement 1.19.2_4158⁷⁰ and manual rebuilding in COOT. The quality of the refined model was analyzed by MolProbity integrated into Phenix⁷¹ with statistics reported in Table 1. Figures were prepared using UCSF ChimeraX⁶⁵.

Molecular dynamics simulations and interface energy calculations

The cryo-EM structure of the MT-U-2 LIS1 complex was prepared before modeling and simulations in Charmm-GUI⁷². The large-scale Atomic/Molecular Massively Parallel Simulator was applied for the simulations⁷³. Periodic boundary conditions were used to produce a series of proteins. Amber10:EHT force field (<https://infoscience.epfl.ch/record/121435/files/Amber10i.pdf>) was used to simulate proteins.

Water molecules were simulated using the rigid SPC/E force field⁷⁴, and the SHAKE algorithm⁷⁵ was used to keep the water molecules rigid throughout the entire simulation. The Lennard-Jones 12-6 term⁷⁶ was used to describe the short-range interactions, and the cutoff distance was 12 Å. The particle-particle/particle-mesh method with a precision value of 10^{−6} was used to estimate long-range electrostatic interactions⁷⁷. First, we ran the energy minimization for the whole system. Next, the simulations were carried out at 25 °C using a canonical NVT ensemble, where the temperature was controlled by the Nosé-Hoover thermostat⁷⁸. Then NPT ensemble was performed in production phase, where the target pressure and temperature were 1 atm and 25 °C, respectively. Default tether restraints from LAMMPS were applied to the system.

Protein models after in silico mutations underwent the same preparation procedure. Interface energy was calculated in the production phase. The interface energy calculation between contacting residue pairs was processed. The proximity threshold was set to 12 Å. Atoms separated by more than this distance were not considered to be interacting. Six types of contacts were identified: hydrogen bonds, metal, ionic, arene, covalent and Van der Waals distance interactions.

Figure preparation

Figures and plots were prepared using GraphPad Prism 9.0, MP Discover (for mass photometry data), FIJI/ImageJ (for light microscopy images), UCSF ChimeraX 1.4, and Adobe Illustrator 27.1.1.

Statistics and reproducibility

All data were collected from at least two independent replicates (independent protein preparations, or cell cultures, for in vitro and in vivo experiments, respectively). All phenotypes were also validated in at least two biological replicates for in vivo experiments. The values from each independent replicate showed similar results. *t*-tests were performed using GraphPad Prism. Statistical significance was determined using an ANOVA with Dunnett's multiple comparison test, or by calculating *Z* scores using the following formula, where *y* is number of observations, and *n* is sample size:

$$Z = \frac{(\hat{p}_1 - \hat{p}_2)}{\hat{p}(1 - \hat{p})\left(\frac{1}{n_1} + \frac{1}{n_2}\right)}$$

where:

$$\hat{p} = \frac{y_1 + y_2}{n_1 + n_2}$$

Z scores were converted to two-tailed *P* values using an online calculator.

Reporting summary

Further information on research design is available in the Nature Portfolio Reporting Summary linked to this article.

Data availability

Models and cryo-EM maps have been deposited in the PDB and EMD as follows: PDB 8FCY and EMD-28999 (dynein_{MOTOR}^{MT-B} in ATP), PDB 8FD6 and EMD-29003 (dynein_{MOTOR}^{MT-U} in ATP and Vi), PDB 8FDT and EMD-29012 (dynein_{MOTOR}^{MT-U} + LIS1 in ATP and Vi), and PDB 8FDU and EMD-29014 (dynein_{MOTOR}^{MT-U} + LIS1 in ATP and Vi, locally refined at AAA3-AAA5 with 2 LIS1s). Residues labeled in the figures for human dynein are based on the Cytoplasmic Dynein-1 Heavy Chain 1 sequence (Q14204). All of the plasmids, yeast strains, datasets and raw video files that were generated during and/or analyzed during this study are available from the corresponding authors upon request. All data used to generate plots throughout the manuscript are included as Source Data files,

as are raw images of uncropped gels. PDB models used throughout this study include 5NUG (ref. 3), 4RH7 (ref. 37), 7MGM (ref. 39), 8DYU (ref. 41), 7ZG8 (ref. 38), 3VKG (ref. 79), 4AKG (ref. 80), 4W8F (ref. 81), and 1UUJ (ref. 82). Source data are provided with this paper.

References

52. Bi, E. & Pringle, J. R. *ZDS1* and *ZDS2*, genes whose products may regulate Cdc42p in *Saccharomyces cerevisiae*. *Mol. Cell Biol.* **16**, 5264–5275 (1996).
53. Knop, M. et al. Epitope tagging of yeast genes using a PCR-based strategy: more tags and improved practical routines. *Yeast* **15**, 963–972 (1999).
54. Longtine, M. S. et al. Additional modules for versatile and economical PCR-based gene deletion and modification in *Saccharomyces cerevisiae*. *Yeast* **14**, 953–961 (1998).
55. Markus, S. M., Omer, S., Baranowski, K. & Lee, W. L. Improved plasmids for fluorescent protein tagging of microtubules in *Saccharomyces cerevisiae*. *Traffic* **16**, 773–786 (2015).
56. Gibson, D. G. et al. Enzymatic assembly of DNA molecules up to several hundred kilobases. *Nat. Methods* **6**, 343–345 (2009).
57. Marzo, M. G. et al. Molecular basis for dyneinopathies reveals insight into dynein regulation and dysfunction. *eLife* **8**, e47246 (2019).
58. Ecklund, K. H. et al. She1 affects dynein through direct interactions with the microtubule and the dynein microtubule-binding domain. *Nat. Commun.* **8**, 2151 (2017).
59. Cheng, K., Wilkinson, M., Chaban, Y. & Wigley, D. B. A conformational switch in response to Chi converts RecBCD from phage destruction to DNA repair. *Nat. Struct. Mol. Biol.* **27**, 71–77 (2020).
60. Mastrorade, D. N. Automated electron microscope tomography using robust prediction of specimen movements. *J. Struct. Biol.* **152**, 36–51 (2005).
61. Punjani, A., Rubinstein, J. L., Fleet, D. J. & Brubaker, M. A. cryoSPARC: algorithms for rapid unsupervised cryo-EM structure determination. *Nat. Methods* **14**, 290–296 (2017).
62. Bepko, T. et al. Positive-unlabeled convolutional neural networks for particle picking in cryo-electron micrographs. *Nat. Methods* **16**, 1153–1160 (2019).
63. Punjani, A., Zhang, H. & Fleet, D. J. Non-uniform refinement: adaptive regularization improves single-particle cryo-EM reconstruction. *Nat. Methods* **17**, 1214–1221 (2020).
64. Tan, Y. Z. et al. Addressing preferred specimen orientation in single-particle cryo-EM through tilting. *Nat. Methods* **14**, 793–796 (2017).
65. Goddard, T. D. et al. UCSF ChimeraX: meeting modern challenges in visualization and analysis. *Protein Sci.* **27**, 14–25 (2018).
66. Kidmose, R. T. et al. Namdinator — automatic molecular dynamics flexible fitting of structural models into cryo-EM and crystallography experimental maps. *IUCr* **6**, 526–531 (2019).
67. Casanál, A., Lohkamp, B. & Emsley, P. Current developments in Coot for macromolecular model building of electron cryo-microscopy and crystallographic Data. *Protein Sci.* **29**, 1069–1078 (2020).
68. Brown, A. et al. Tools for macromolecular model building and refinement into electron cryo-microscopy reconstructions. *Acta Crystallogr. D Biol. Crystallogr.* **71**, 136–153 (2015).
69. Jumper, J. et al. Highly accurate protein structure prediction with AlphaFold. *Nature* **596**, 583–589 (2021).
70. Afonine, P. V. et al. Real-space refinement in PHENIX for cryo-EM and crystallography. *Acta Crystallogr. D Struct. Biol.* **74**, 531–544 (2018).
71. Chen, V. B. et al. MolProbity: all-atom structure validation for macromolecular crystallography. *Acta Crystallogr. D Biol. Crystallogr.* **66**, 12–21 (2010).
72. Jo, S., Kim, T., Iyer, V. G. & Im, W. CHARMM-GUI: a web-based graphical user interface for CHARMM. *J. Comput. Chem.* **29**, 1859–1865 (2008).
73. Thompson, A. et al. LAMMPS — a flexible simulation tool for particle-based materials modeling at the atomic, meso, and continuum scales. *Comput. Phys. Commun.* **271**, 108171 (2022).
74. Berendsen, H., Van Gunsteren, W., Egberts, E. & De Vlieg, J. Dynamic simulation of complex molecular systems. *Supercomputer Res. Chem. Chem. Eng.* **353**, 106–122 (1987).
75. Ryckaert, J.-P., Ciccotti, G. & Berendsen, H. Numerical integration of the cartesian equations of motion of a system with constraints: molecular dynamics of *n*-alkanes. *J. Computational Phys.* **23**, 327–341 (1977).
76. Jones, J. E. & Ingham, A. E. On the calculation of certain crystal potential constants, and on the cubic crystal of least potential energy. *Proc. R. Soc. A* **107**, 636–653 (1925).
77. Hockney, R. W. & Eastwood, J. W. *Computer Simulation Using Particles* (CRC Press, 1988).
78. Evans, D. J. & Holian, B. L. The nose–hoover thermostat. *J. Chem. Phys.* **83**, 4069–4074 (1985).
79. Kon, T. et al. The 2.8-Å crystal structure of the dynein motor domain. *Nature* **484**, 345–350 (2012).
80. Schmidt, H., Gleave, E. S. & Carter, A. P. Insights into dynein motor domain function from a 3.3-Å crystal structure. *Nat. Struct. Mol. Biol.* **19**, 492–497 (2012). S491.
81. Bhabha, G. et al. Allosteric communication in the dynein motor domain. *Cell* **159**, 857–868 (2014).
82. Kim, M. H. et al. The structure of the N-terminal domain of the product of the lissencephaly gene *Lis1* and its functional implications. *Structure* **12**, 987–998 (2004).

Acknowledgements

We are very grateful to Janelia Research Campus for providing fluorescent Halo and SNAP dyes, A. Carter and S. Chabaa for valuable discussions (and for sharing data that was unpublished at the time), and to members of the Markus and DeLuca laboratories for valuable discussions. This work was funded by the NIH/NIGMS (R35GM139483 to S.M.M., and R35GM142959 to K.Z.) and in part by a Collaboration Development Award Program from the Pittsburgh Center for HIV Protein Interactions (U54AI170791 to K.Z.). The funders had no role in study design, data collection and analysis, decision to publish, or preparation of this manuscript. We would like to thank K. Zhou and J. Lin for the help with cryo-EM data collection at Yale ScienceHill-Cryo-EM facility. The Yale Cryo-EM Resource is funded in part by the NIH grant S10OD023603. We thank L. Wang, J. Kaminsky, and G. Hu at the Laboratory for BioMolecular Structure (LBMS) for help with cryo-EM data collection. The LBMS is supported by the DOE Office of Biological and Environmental Research (KP1607011).

Author contributions

S.M.M. designed the study. W.D.T., C.B.-P., N.T.F., L.G.L., and S.M.M. purified yeast proteins, and W.D.T., C.B.-P., and S.M.M. purified human proteins. L.G.L. performed ATPase assays with MT-U and MT-B proteins. W.D.T., N.T.F. and S.M.M. performed in vitro binding assays. W.D.T., N.T.F., L.G.L., and S.M.M. performed and analyzed live-cell microscopy. Y.W. and P.C. acquired and analyzed cryo-EM data, and built PDB models with support from K.Z. H.X., and Y.C. performed molecular dynamics simulations. S.M.M., Y.W., P.C., L.G.L., and S.M.M. generated figures. S.M.M. wrote the manuscript. W.D.T., Y.C., P.C., K.Z., and S.M.M. edited and revised the manuscript. S.M.M. and K.Z. acquired funding.

Competing interests

The authors declare no competing interests.

Additional information

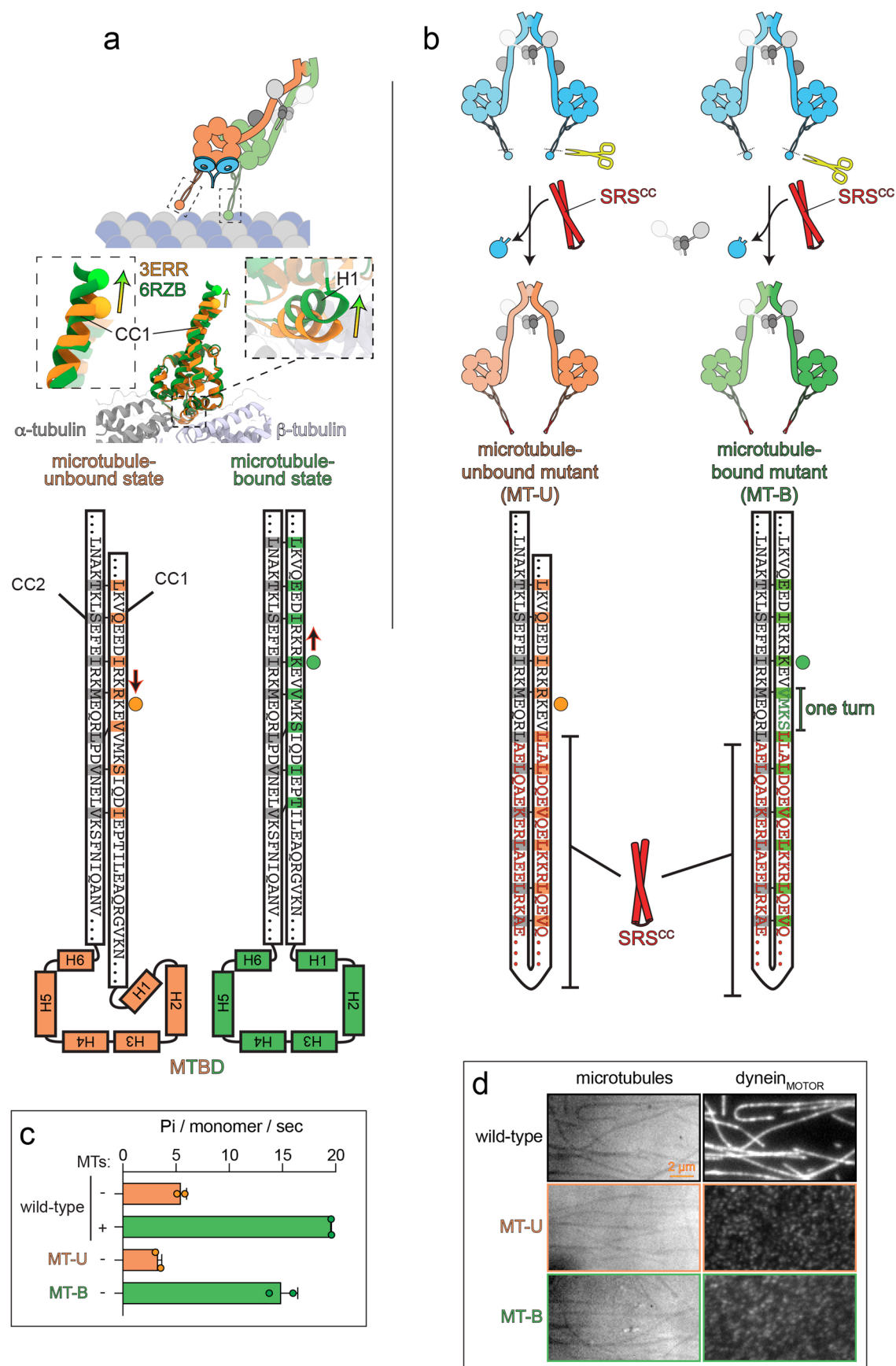
Extended data is available for this paper at <https://doi.org/10.1038/s41594-023-01010-x>.

Supplementary information The online version contains supplementary material available at <https://doi.org/10.1038/s41594-023-01010-x>.

Correspondence and requests for materials should be addressed to Kai Zhang or Steven M. Markus.

Peer review information *Nature Structural & Molecular Biology* thanks Arne Gennerich, Clinton Lau and the other, anonymous, reviewer(s) for their contribution to the peer review of this work. Primary Handling Editor: Katarzyna Ciazynska, in collaboration with the *Nature Structural & Molecular Biology* team. Peer reviewer reports are available.

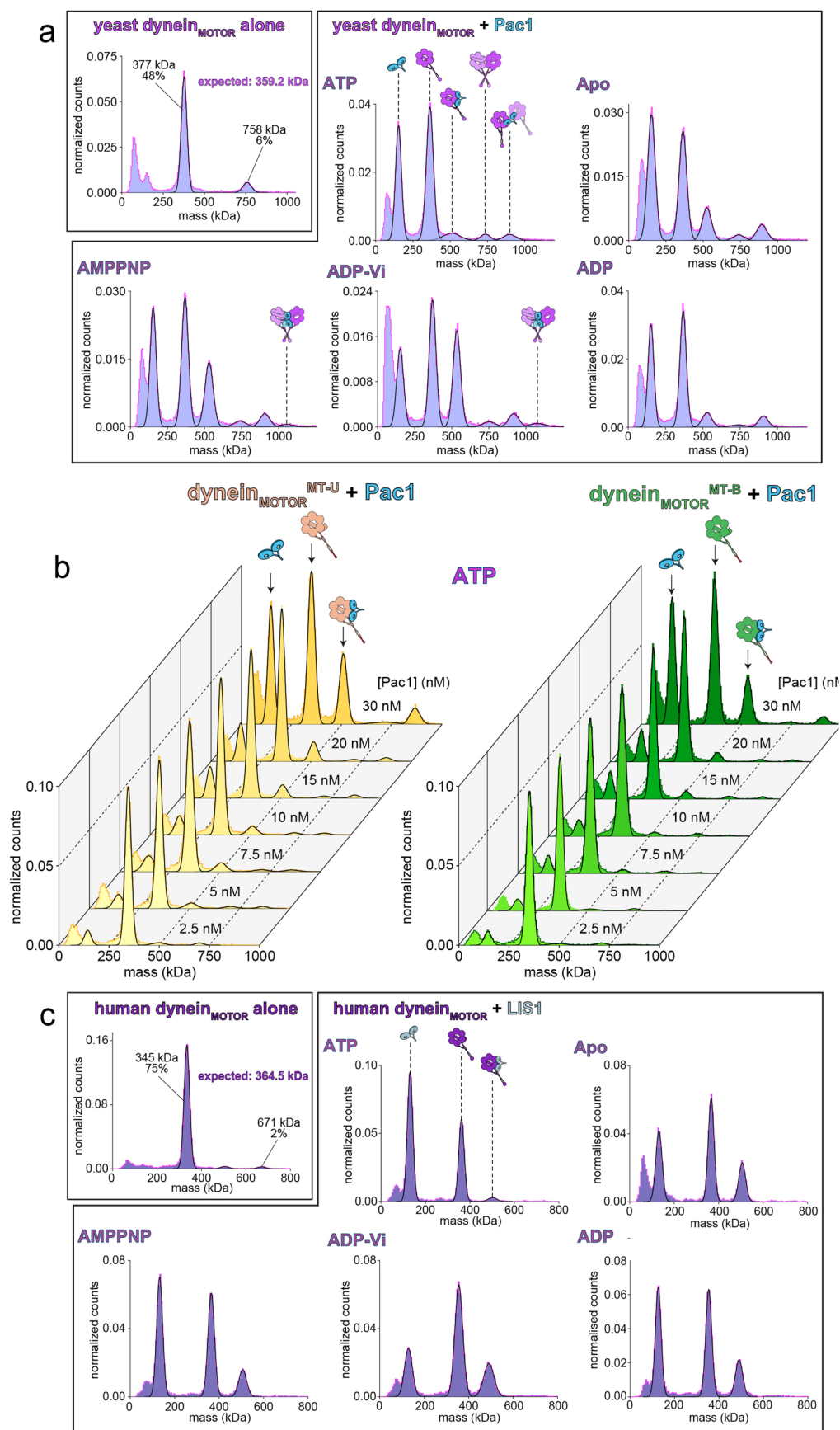
Reprints and permissions information is available at www.nature.com/reprints.



Extended Data Fig. 1 | See next page for caption.

Extended Data Fig. 1 | Design strategy and validation of microtubule-bound and -unbound dynein mutants. (a) Cartoon and structural depiction of conformational change that takes place within the coiled-coil (CC) stalk and microtubule-binding domain (MTBD) upon microtubule binding. Comparison of a high resolution microtubule-bound dynein MTBD (6RZB)³⁰ and a crystal structure of a microtubule unbound MTBD (3ERR)³² reveals an upward shift of helix 1 (H1) as a result of microtubule binding. This results in a consequent upward shift of CC1 with respect to CC2. (b) Design strategy to generate constitutive microtubule-unbound and -bound dynein mutants. The stable coiled-coil from seryl tRNA synthetase (SRS^{CC}) was used to replace the entire dynein MTBD plus short regions of CC1 and CC2. The MT-B mutant has 4 additional residues in CC1 with respect to the MT-U mutant (corresponding to

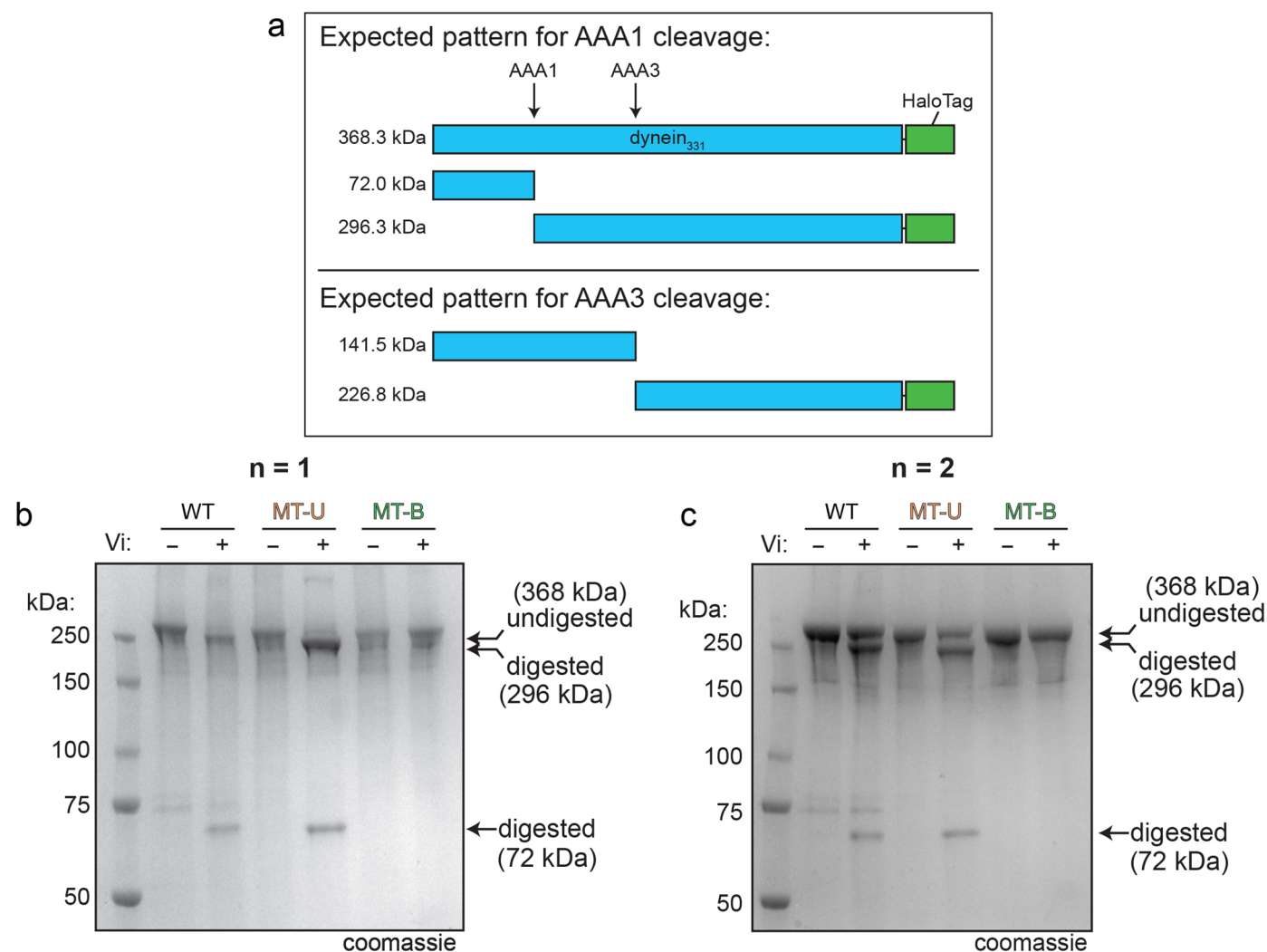
one helix turn), resulting in a presumed upward shift of CC1 compared to CC2. (c) Plot (mean \pm SD, along with individual data points) depicting ATPase levels for artificially dimerized dynein motor domain fragments (GST-dynein_{MOTOR}; n = 2 independent replicates for each). Note the MT-U mutant closely reflects the wild-type dynein motor in the absence of microtubules, while the MT-B mutant matches that of wild-type plus a saturating concentration of microtubules (2 μ M)³⁸. (d) Representative images (fluorescence for dynein_{MOTOR} fragments, and interference reflection microscopy for microtubules) showing the ability of wild-type, but not dynein^{MT-U} or dynein^{MT-B}, to bind microtubules (images are representative of 2 independent replicates). Coverslip-immobilized microtubules were incubated with 50 nM of indicated dynein_{MOTOR} fragments (labeled via C-terminal HaloTag^{IFX646}) prior to imaging.



Extended Data Fig. 2 | See next page for caption.

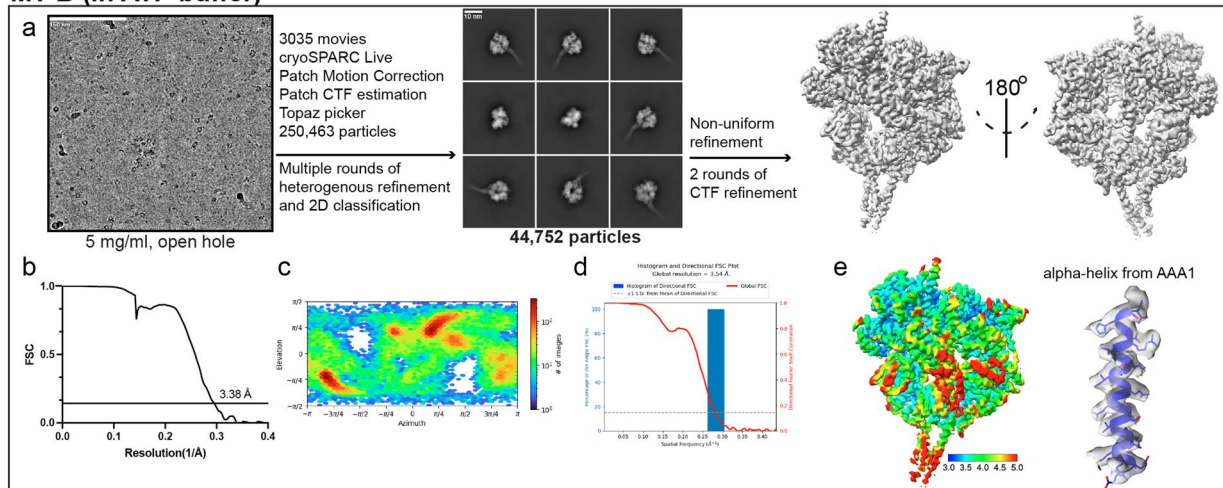
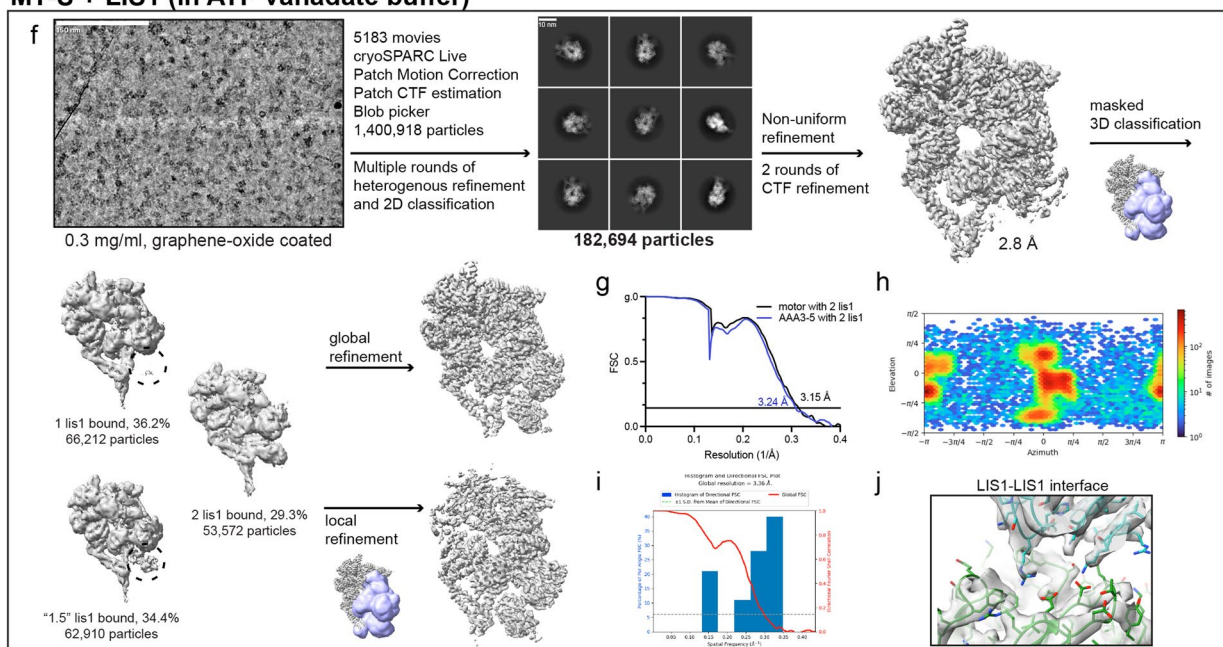
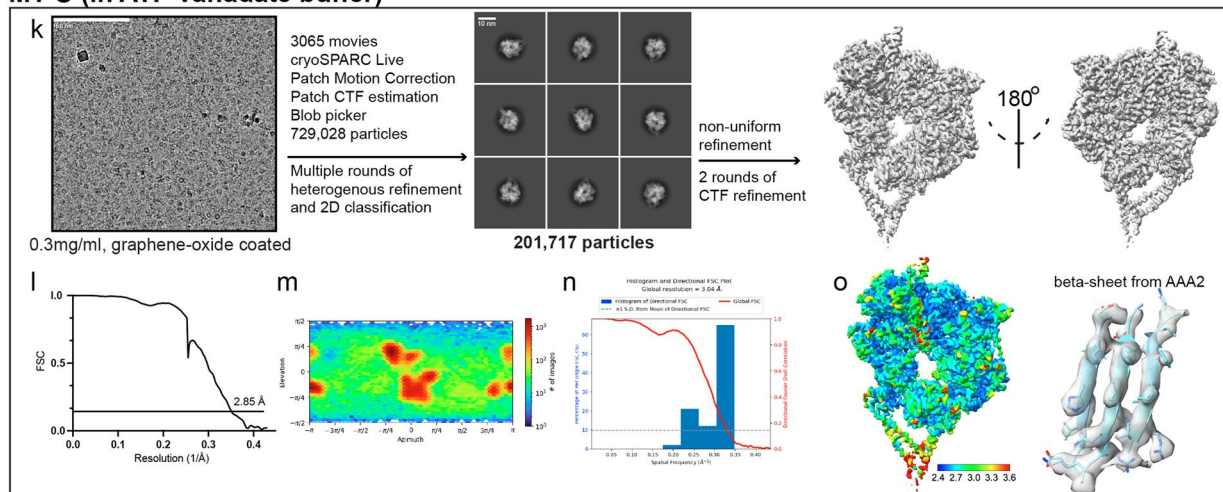
Extended Data Fig. 2 | Additional mass photometric analysis of Pac1- and LIS1-dynein_{MOTOR} binding. (a) Representative mass histograms for wild-type yeast dynein_{MOTOR} with and without Pac1 with different nucleotides, as indicated (see Fig. 3 and Methods). Cartoon depictions above peaks indicate the likely dynein_{MOTOR}-Pac1 complex contained therein. (b) Histograms from mass photometry analysis depicting relative dynein_{MOTOR}-Pac1 complex

formation in the presence of a fixed concentration of each motor (25 nM) and increasing concentrations of Pac1 (as indicated). Note the higher fraction of dynein_{MOTOR}^{MT-U}-Pac1 complex formation with respect to dynein_{MOTOR}^{MT-B}-Pac1 at every concentration. (c) Representative mass histograms for wild-type human dynein_{MOTOR} with and without LIS1 with different nucleotides, as indicated.



Extended Data Fig. 3 | Vanadate-mediated photocleavage assay. (a) Schematic depicting expected vanadate-mediated photocleavage if vanadate were bound to AAA1 (top) or AAA3 (bottom). (b and c) Two independent replicates

of photocleavage assay. Purified indicated yeast dynein_{MOTOR} fragments were incubated with 3 mM ATP with or without 3 mM vanadate, exposed to ultraviolet light (254 nm) for 1 hour, and then analyzed by coomassie-stained SDS-PAGE.

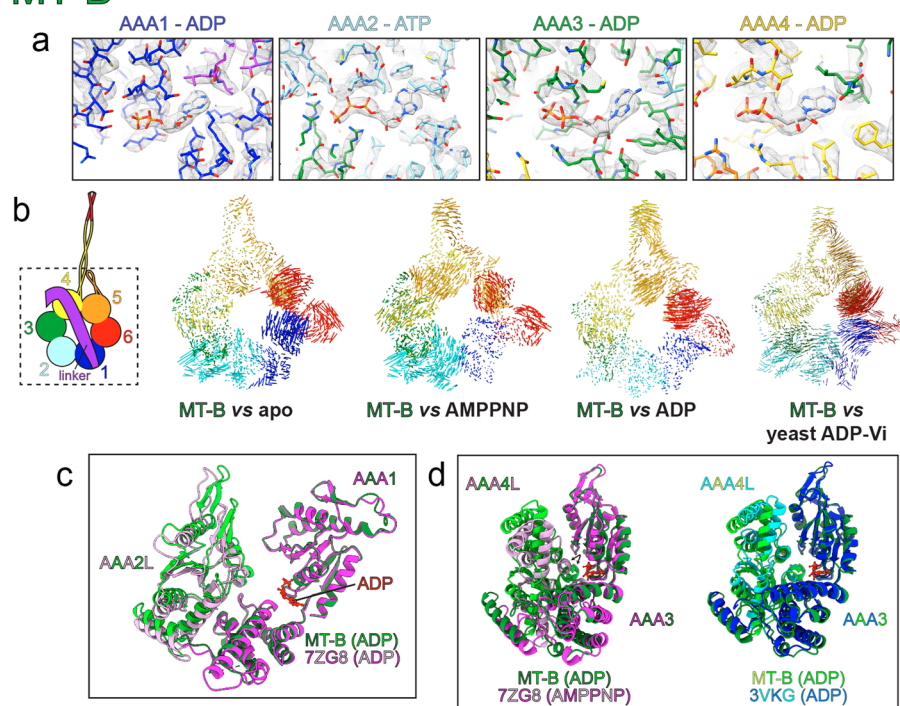
MT-B (in ATP buffer)**MT-U + LIS1 (in ATP vanadate buffer)****MT-U (in ATP vanadate buffer)**

Extended Data Fig. 4 | See next page for caption.

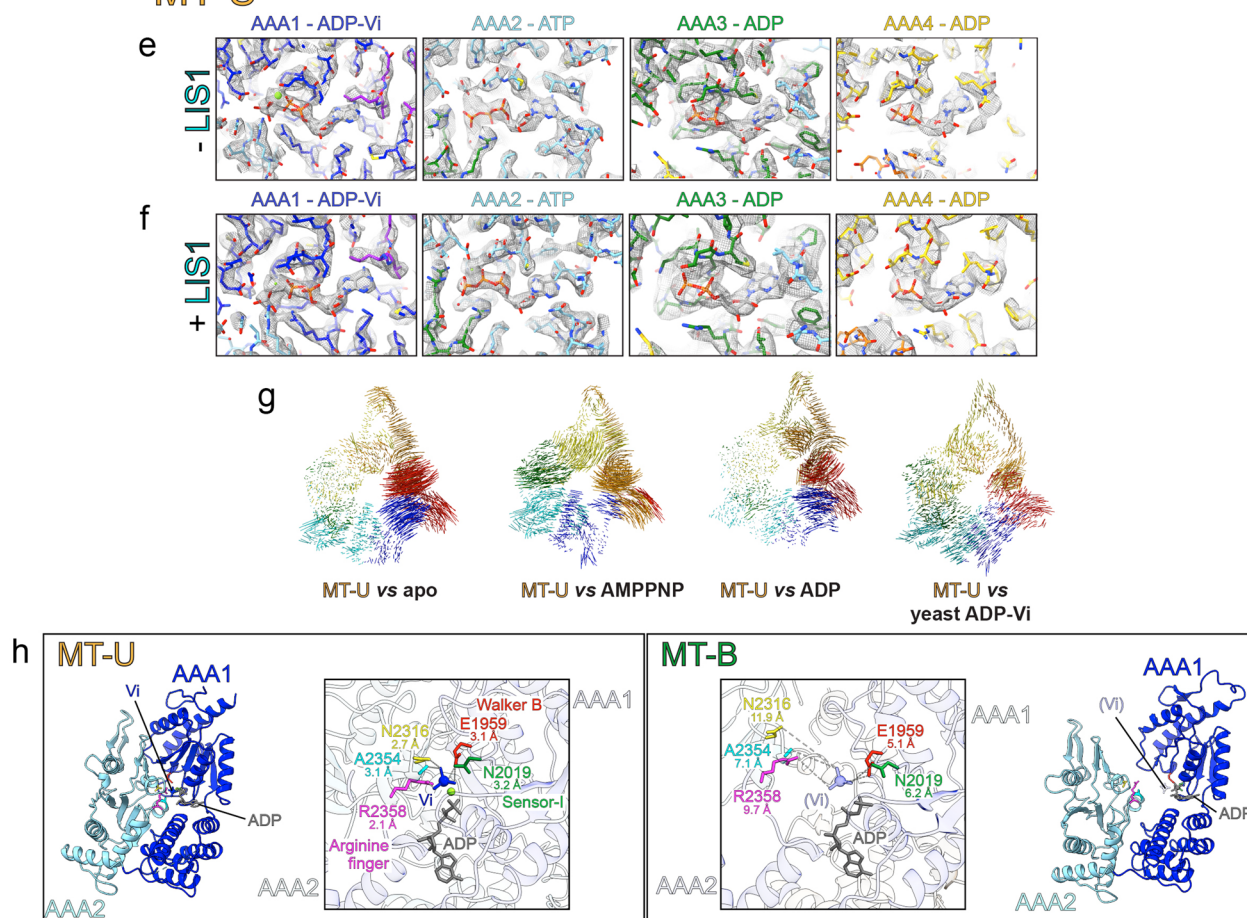
Extended Data Fig. 4 | Cryo-EM data processing flowchart. (a) Cryo-EM workflow of MT-B in the presence of ATP (details in Methods). (b) FSC curves with the gold standard threshold of 0.143 for MT-B. (c, d) Particle distribution plot and 3D FSC analysis of MT-B. (e) Local resolution analysis of MT-B and representative cryo-EM densities. (f) Cryo-EM workflow of MT-U with LIS1. (g) FSC curves with the gold standard threshold of 0.143. (h, i) Particle distribution plot and 3D FSC

analysis of MT-U + LIS1 in the presence of ATP and Vi. (j) Local resolution analysis and representative cryo-EM densities of the LIS1-LIS1 interface. (k) Cryo-EM workflow of MT-U alone in the presence of ATP and Vi. (l) FSC curves with the gold standard threshold of 0.143. (m, n) Particle distribution plot and 3D FSC analysis of MT-U. (o) Local resolution analysis and representative cryo-EM densities.

MT-B



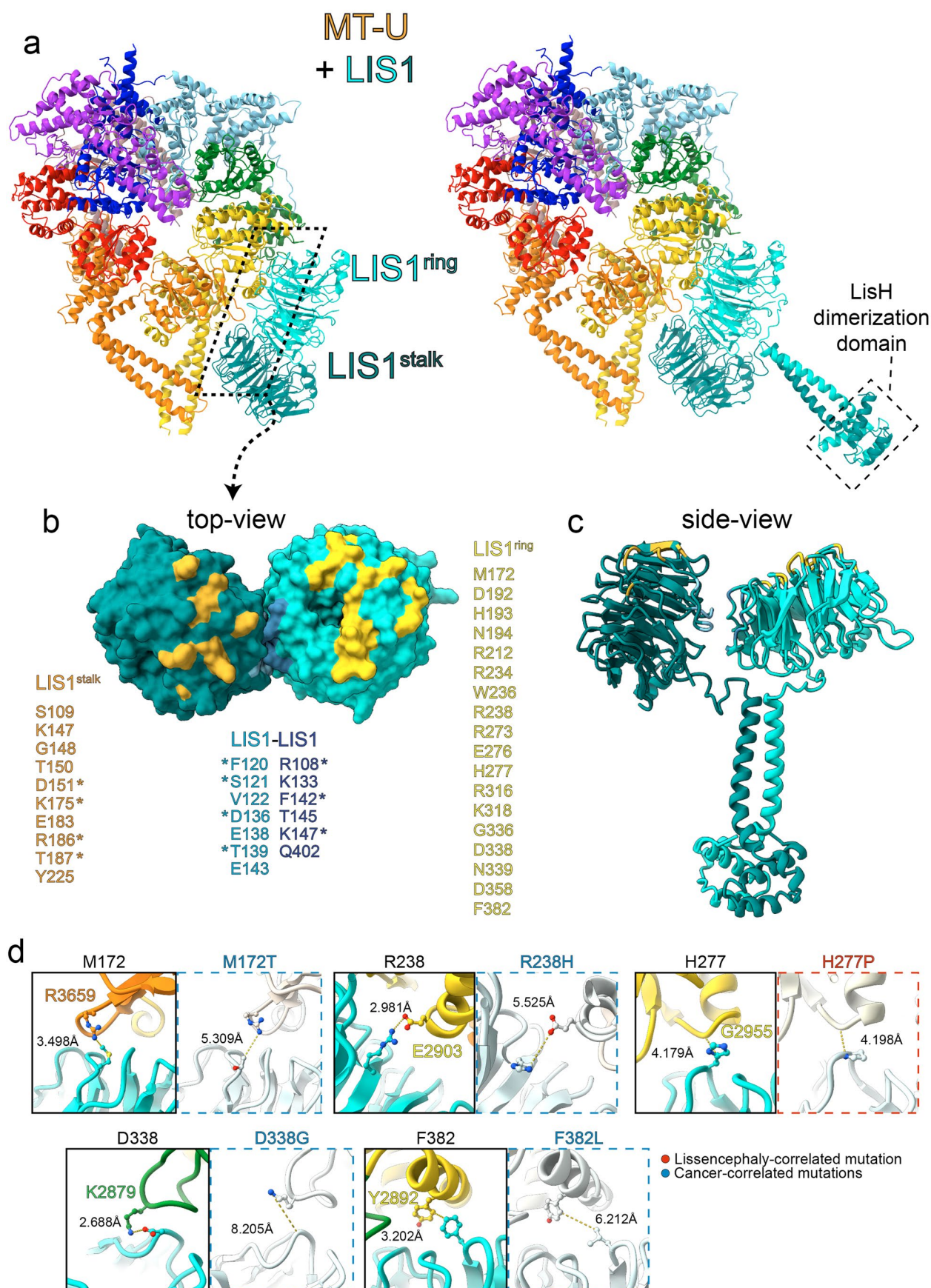
MT-U



Extended Data Fig. 5 | See next page for caption.

Extended Data Fig. 5 | Additional analysis of human MT-U and MT-B cryo-EM structures. (a) Stick representations of the dynein_{MOTOR}^{MT-B} AAA sites showing the nucleotide electron density (the center of each image) and surrounding residues (residues are color-coded as shown in panel b schematic). (b) Vector maps depicting pairwise alpha carbon interatomic distances between the dynein_{MOTOR}^{MT-B} with the following: apo yeast dynein (4AKG), AMPPNP-bound yeast dynein (4W8F), ADP-bound *Dictyostelium discoideum* dynein (3VKG), and ADP-Vi and Pac1-bound yeast dynein (7MGM)^{37,40,79,81}. Structures were globally aligned after removal of the linkers. (c) AAA1-AAA2L domains from dynein_{MOTOR}^{MT-B} (shades of green) and the native microtubule-bound dynein-1 (7Z8G; magenta and pink) overlaid to depict the high degree of structural similarity. The two were locally aligned using AAA1. (d) AAA3-AAA4L domains from dynein_{MOTOR}^{MT-B} (shades of green) overlaid with either the native

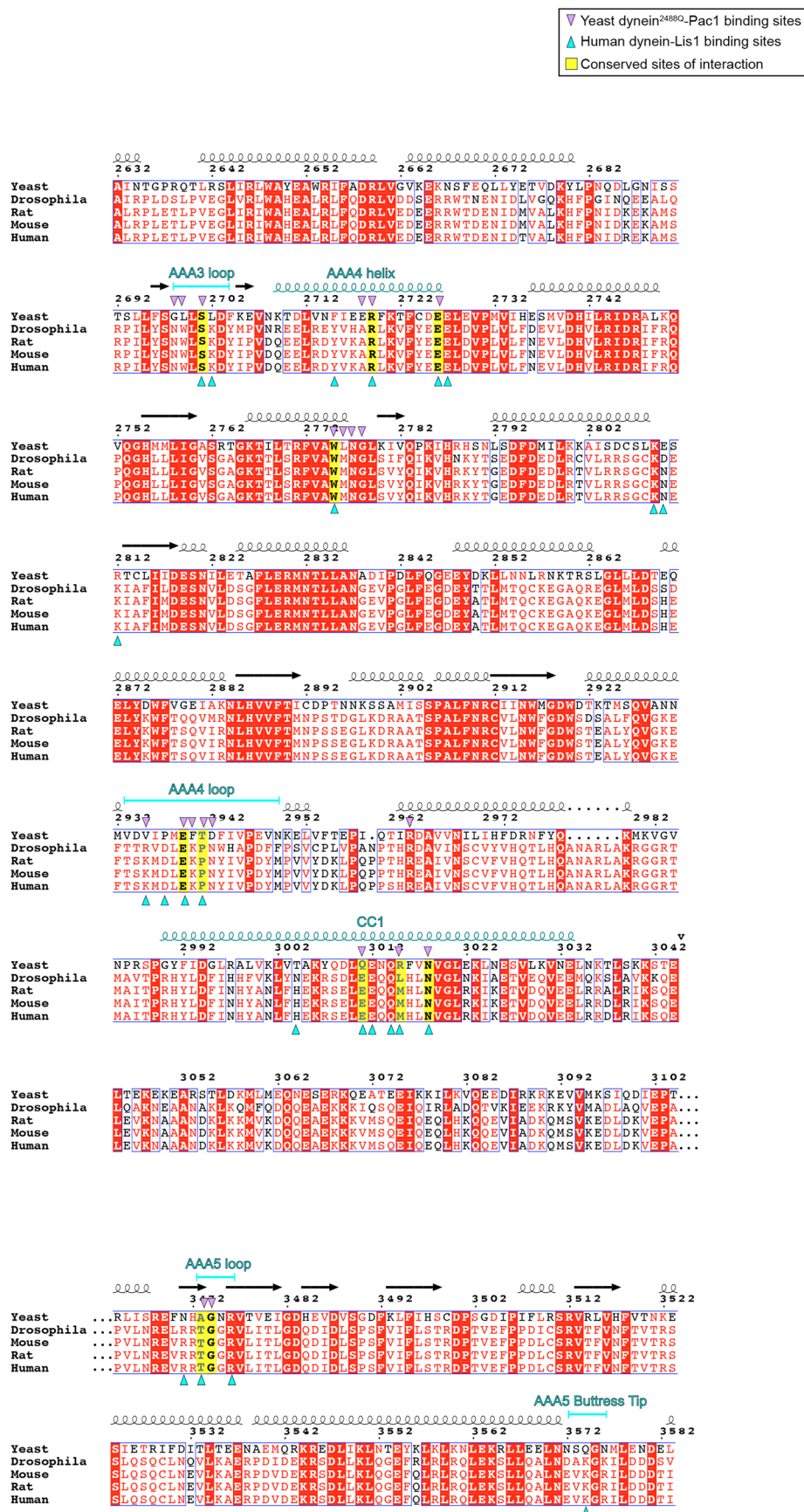
microtubule-bound dynein-1 (left, magenta and pink) or the ADP-bound *Dictyostelium discoideum* dynein (right, blue and green). (e and f) Stick representations of the LIS1-unbound (e) or bound (f) dynein_{MOTOR}^{MT-U} AAA sites showing the nucleotide electron density and surrounding residues (residues are color-coded as shown in panel b schematic). (g) Vector maps depicting pairwise alpha carbon interatomic distances between the LIS1-bound dynein_{MOTOR}^{MT-U} with those described for panel b. Structures were globally aligned after removal of the linkers. (h) AAA1-AAA2L domains from dynein_{MOTOR}^{MT-U} (left) and dynein_{MOTOR}^{MT-B} (right) with residues of dynein_{MOTOR}^{MT-U} contacting the Vi highlighted (E19S9, Walker B; N2019, Sensor-I; R2358, arginine finger; N2316; A2354;). Distances between these residues and the Vi (or, for the dynein_{MOTOR}^{MT-B} structure, between them and where the Vi would be) are indicated.

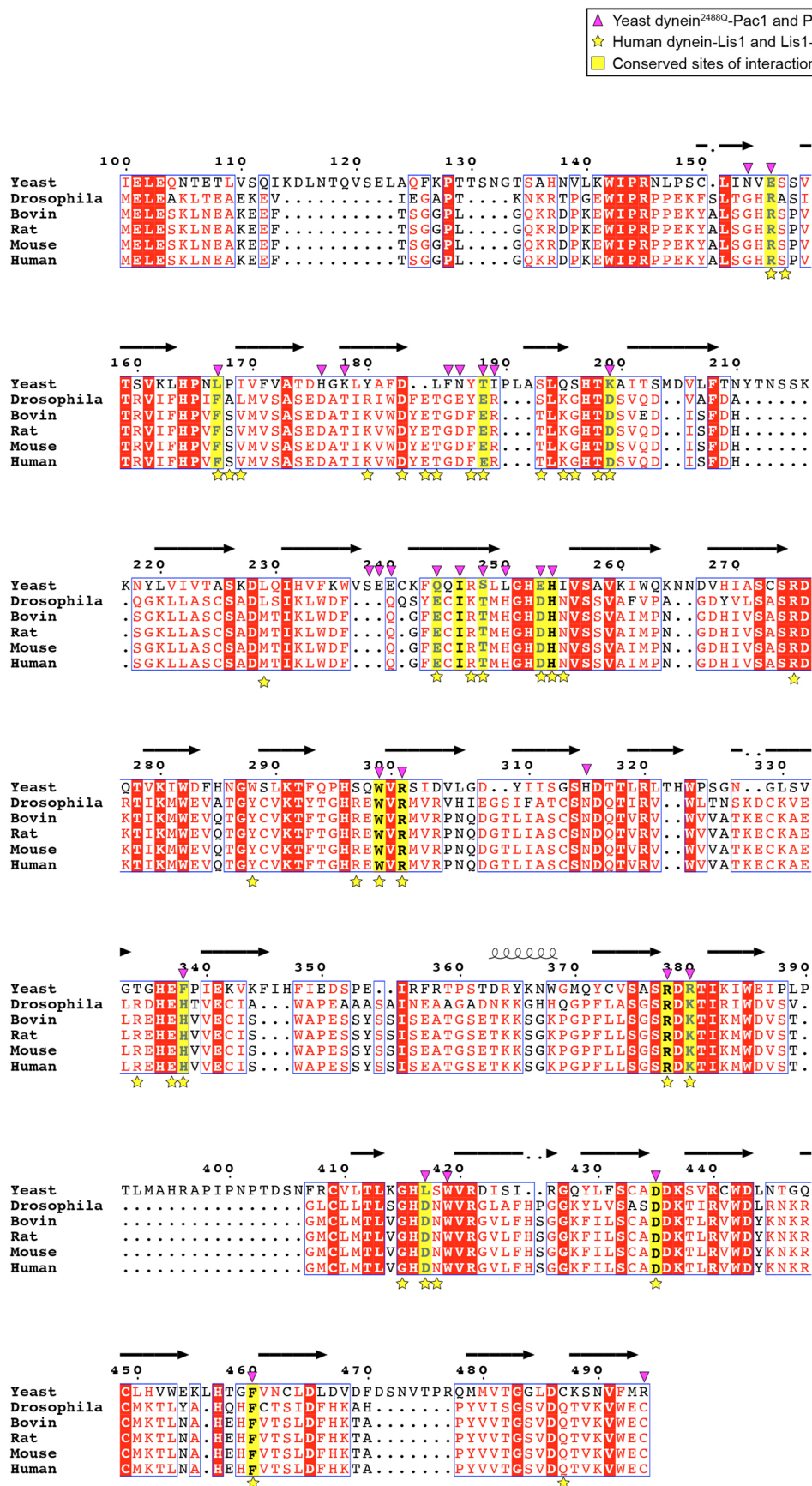


Extended Data Fig. 6 | See next page for caption.

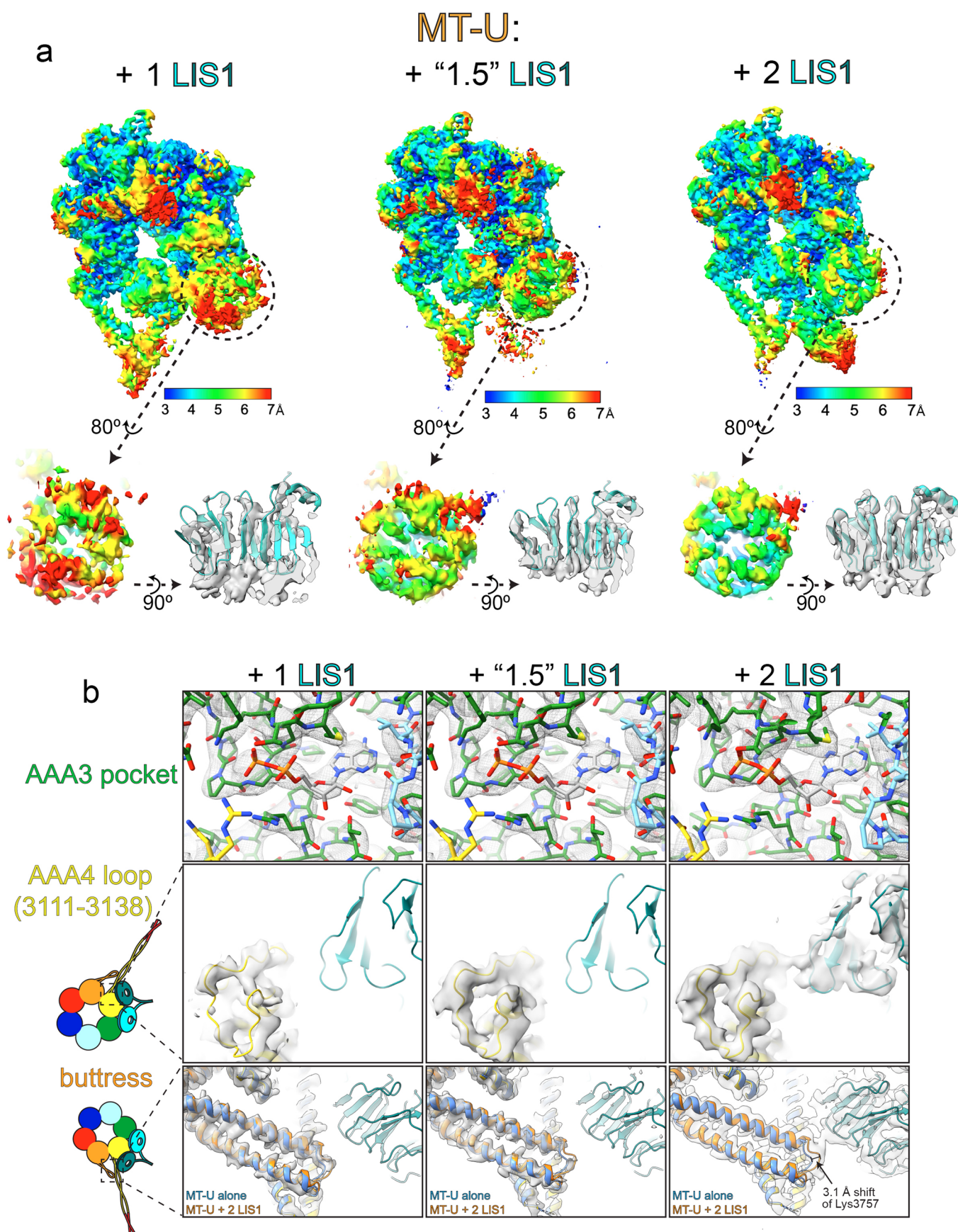
Extended Data Fig. 6 | Additional analysis of LIS1-bound dynein_{MOTOR}^{MT-U} structure. (a) 2 LIS1-bound dynein_{MOTOR}^{MT-U} structure with domains colored as shown in Fig. 5 (left) and the same shown with the full-length LIS1 homodimer, with the N-terminal dimerization domain modeled. The LIS1 N-terminal dimer model was generated using a combination of AlphaFold prediction⁶⁹ and a previous crystal structure, 1UUJ⁸². The structure was manually adjusted in COOT. (b) View of LIS1 homodimer surface that contacts site^{stalk} (teal) and site^{ring} (cyan).

Residues listed and indicated in different colors on the structure are those that make direct contact with dynein or LIS1. Residues with “*” are those identified in a recent study to make contact with wild-type human dynein⁴¹. (c) Side-view of full-length LIS1 homodimer model with residues colored as in panel b. (d) Results of molecular dynamics simulation from Fig. 5g depicting change in interatomic distances in residues mediating contacts between LIS1 and dynein as a consequence of indicated mutations.





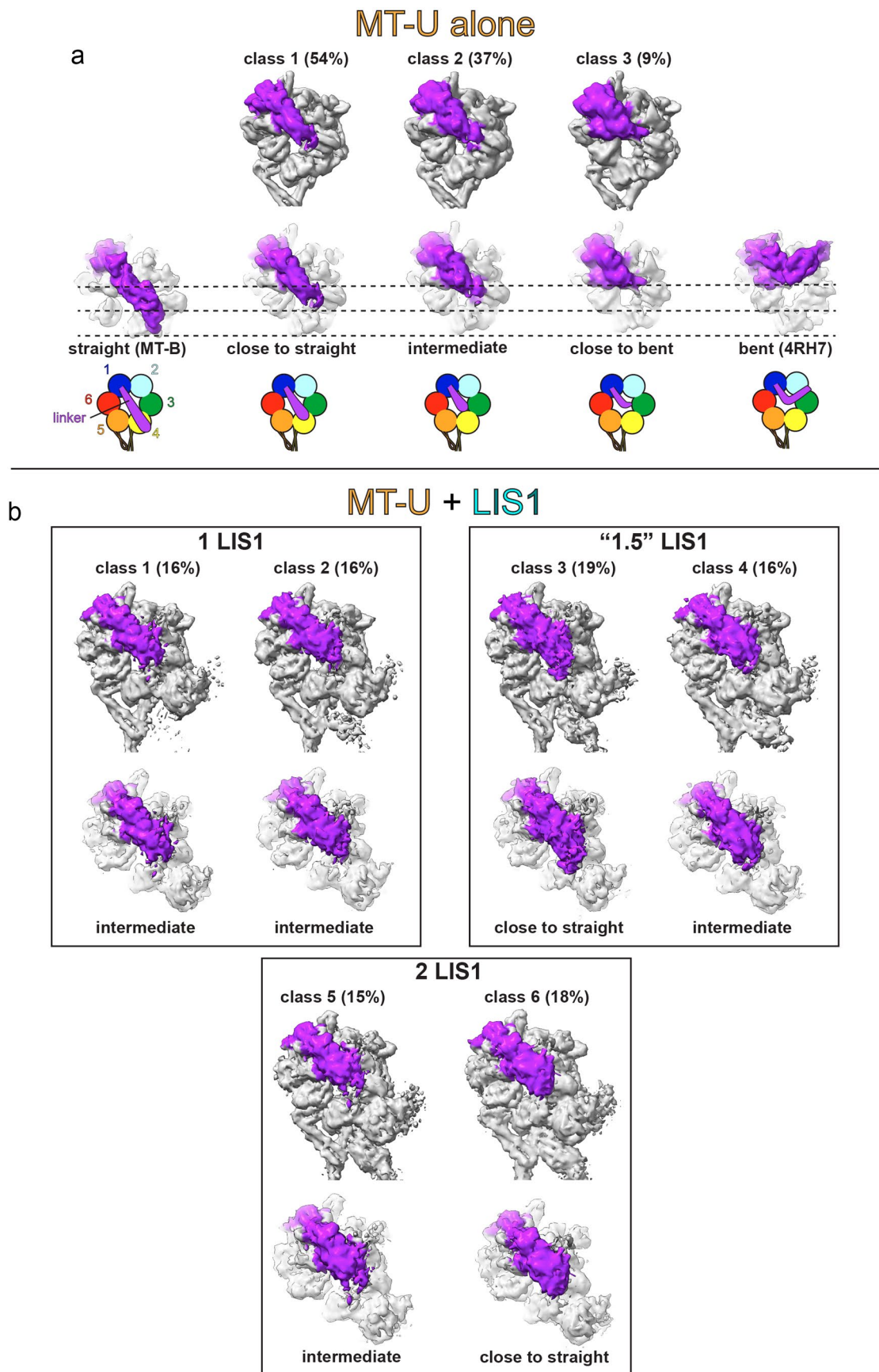
Extended Data Fig. 8 | Sequence alignment of dynein-binding regions within LIS1 and homologs. Numbering corresponds to yeast Pac1 sequence. Secondary structure indicated with cartoon helices (for alpha-helices) and arrows (for beta-strands).



Extended Data Fig. 9 | See next page for caption.

Extended Data Fig. 9 | 3D classification analysis of LIS1-bound dynein_{MOTOR}^{MT-U} structures. (a) The three classes of LIS1-bound dynein (shown with a rotated close-up view of LIS1^{ring}) are shown with local resolution indicated by color. Note the significant increase in resolution and map quality for LIS1^{ring} for the '1.5' and 2 LIS1-bound dyneins. (b) Close-up views of the indicated regions of the LIS1-bound

dynein_{MOTOR}^{MT-U} structure. Note all three structures have clear density for ADP at AAA3 (top), and there is an improvement in local resolution for the AAA4 loop (middle) and the buttress for the '1.5' and 2 LIS1-bound structures. EM densities of each 3D class are shown along with models of dynein_{MOTOR}^{MT-U} and dynein_{MOTOR}^{MT-U} + 2 LIS1 for comparison in bottom two rows.



Extended Data Fig. 10 | See next page for caption.

Extended Data Fig. 10 | 3D classification reveals flexibility of MT-U linker that is independent of LIS1 binding. (a) 3D classification results for MT-U alone. Front views of the motor, and zoomed-in views of the linker (colored in purple) are shown. The linker position is indicated in the cartoon model. The map contour levels are all set to 0.45. Note that no obvious bent linker was observed

in any class. (b) 3D classification results of MT-U with LIS1. The classification is mainly guided by LIS1 occupancy, but the linker flexibility can also be visualized at low map contour levels (all set to 0.2). For all classes, the linker position is flexible. No obvious bent linker was observed regardless of LIS1 occupancy.

Reporting Summary

Nature Portfolio wishes to improve the reproducibility of the work that we publish. This form provides structure for consistency and transparency in reporting. For further information on Nature Portfolio policies, see our [Editorial Policies](#) and the [Editorial Policy Checklist](#).

Statistics

For all statistical analyses, confirm that the following items are present in the figure legend, table legend, main text, or Methods section.

n/a Confirmed

- ☐ ☒ The exact sample size (n) for each experimental group/condition, given as a discrete number and unit of measurement
- ☐ ☒ A statement on whether measurements were taken from distinct samples or whether the same sample was measured repeatedly
- ☐ ☒ The statistical test(s) used AND whether they are one- or two-sided
Only common tests should be described solely by name; describe more complex techniques in the Methods section.
- ☒ ☐ A description of all covariates tested
- ☐ ☒ A description of any assumptions or corrections, such as tests of normality and adjustment for multiple comparisons
- ☐ ☒ A full description of the statistical parameters including central tendency (e.g. means) or other basic estimates (e.g. regression coefficient) AND variation (e.g. standard deviation) or associated estimates of uncertainty (e.g. confidence intervals)
- ☐ ☒ For null hypothesis testing, the test statistic (e.g. F , t , r) with confidence intervals, effect sizes, degrees of freedom and P value noted
Give P values as exact values whenever suitable.
- ☒ ☐ For Bayesian analysis, information on the choice of priors and Markov chain Monte Carlo settings
- ☒ ☐ For hierarchical and complex designs, identification of the appropriate level for tests and full reporting of outcomes
- ☒ ☐ Estimates of effect sizes (e.g. Cohen's d , Pearson's r), indicating how they were calculated

Our web collection on [statistics for biologists](#) contains articles on many of the points above.

Software and code

Policy information about [availability of computer code](#)

Data collection

For fluorescence microscope control: NIS Elements 5.21.03 (Build 1489)
For mass photometer control: MP Acquire
For cryo-EM data collection and microscope control: SerialEM 3.8 and EPU 2.11.

Data analysis

For Cryo-EM data processing: cryoSPARC Live and cryoSPARC v3.2.
For model building and refinement: ChimeraX 1.4, Namdinator v1, COOT v0.9.5, AlphaFold2 and Phenix 1.19.2_4158.
For fluorescence image analysis: FIJI/ImageJ 2.3.0/1.53f
For mass photometer data analysis: MP Discover
For molecular dynamics simulation and interface energy calculations: Charmm-GUI v1.9, LAMMPS(23Jun 2022), SHAKE algorithm
For figure rendering: ChimeraX 1.4, Adobe Illustrator 27.1.1, and Graphad Prism 9.

For manuscripts utilizing custom algorithms or software that are central to the research but not yet described in published literature, software must be made available to editors and reviewers. We strongly encourage code deposition in a community repository (e.g. GitHub). See the Nature Portfolio [guidelines for submitting code & software](#) for further information.

Data

Policy information about [availability of data](#)

All manuscripts must include a [data availability statement](#). This statement should provide the following information, where applicable:

- Accession codes, unique identifiers, or web links for publicly available datasets
- A description of any restrictions on data availability
- For clinical datasets or third party data, please ensure that the statement adheres to our [policy](#)

Atomic models and EM densities have been deposited into the PDB and EMD as follows: 8FCY/EMD-28999 (MT-B in ATP), 8FD6/EMD-29003 (MT-U in ATP and Vi), 8FDT/EMD-29012 (MT-U + LIS1 in ATP and Vi), and 8FDU/EMD-29014 (MT-U + LIS1 in ATP and Vi, locally refined at AAA3-AAA5 and 2 LIS1s). PDB models used throughout this study include 5NUG, 4RH7, 7MGM, 8DYU, 7ZG8, 3VKG, 4AKG, 4W8F, and 1UUJ.

Human research participants

Policy information about [studies involving human research participants and Sex and Gender in Research](#).

Reporting on sex and gender	<input type="text" value="n/a"/>
Population characteristics	<input type="text" value="n/a"/>
Recruitment	<input type="text" value="n/a"/>
Ethics oversight	<input type="text" value="n/a"/>

Note that full information on the approval of the study protocol must also be provided in the manuscript.

Field-specific reporting

Please select the one below that is the best fit for your research. If you are not sure, read the appropriate sections before making your selection.

☒ Life sciences ☐ Behavioural & social sciences ☐ Ecological, evolutionary & environmental sciences

For a reference copy of the document with all sections, see [nature.com/documents/nr-reporting-summary-flat.pdf](https://www.nature.com/documents/nr-reporting-summary-flat.pdf)

Life sciences study design

All studies must disclose on these points even when the disclosure is negative.

Sample size	No predetermined sample sizes were used in the experimental design. Sample sizes were determined on a case-by-case basis, and determination was based in part on the extent of reproducibility, and also to ensure any apparent differences were reflected in the quantification, as determined by statistical tests. All cells used for imaging were imaged on multiple independent occasions to ensure differences noted (if any) were reproducible. Appropriate statistical tests (described within the text) were used to support conclusions.
Data exclusions	For EM averages, particles with low quality (low contrast, ice contamination) were discarded.
Replication	Biochemical assays (e.g., gel filtration-based binding assay), live cell and single molecule microscopy (i.e., mass photometry) assays, cryo-EM sample preparation and 3D reconstruction were reproduced from at least 2 independent datasets collected from samples prepared with different protein purifications (see Figure legends for precise sample size and replicate information). All differences noted between e.g., mutant and wild-type protein or cells were replicated successfully.
Randomization	All biological samples (e.g., proteins, cells) along with additional assay components were aliquoted into small volumes and randomly allocated into different experimental groups. For all imaging experiments (e.g., mass photometry, live-cell imaging, cryo-EM), random fields-of-view were selected for imaging. For analysis of these data, all molecules (for mass photometry) or all cells from a given field-of-view were included in the analysis. For calculation of the Fourier Shell Correlation (FSC), cryo-EM particles were randomly split into two halves using the cryoSPARC software.
Blinding	Although blinding was not used, all phenotypes were corroborated independently after assessment by at least two individuals without prior knowledge of phenotypes.

Reporting for specific materials, systems and methods

We require information from authors about some types of materials, experimental systems and methods used in many studies. Here, indicate whether each material, system or method listed is relevant to your study. If you are not sure if a list item applies to your research, read the appropriate section before selecting a response.

Materials & experimental systems

n/a	Involved in the study
<input type="checkbox"/>	<input checked="" type="checkbox"/> Antibodies
<input type="checkbox"/>	<input checked="" type="checkbox"/> Eukaryotic cell lines
<input checked="" type="checkbox"/>	<input type="checkbox"/> Palaeontology and archaeology
<input checked="" type="checkbox"/>	<input type="checkbox"/> Animals and other organisms
<input checked="" type="checkbox"/>	<input type="checkbox"/> Clinical data
<input checked="" type="checkbox"/>	<input type="checkbox"/> Dual use research of concern

Methods

n/a	Involved in the study
<input checked="" type="checkbox"/>	<input type="checkbox"/> ChIP-seq
<input checked="" type="checkbox"/>	<input type="checkbox"/> Flow cytometry
<input checked="" type="checkbox"/>	<input type="checkbox"/> MRI-based neuroimaging

Antibodies

Antibodies used

Commercially available anti-tubulin antibodies (Accurate chemical & scientific corporation; Cat #: YSRTMCA77G; clone YL1/2) were used to adhere microtubules to the cover glass for single molecule assays. Antibody was diluted 1:50 (to 8 µg/ml) before use. Lot number 147397 used.

Validation

Validation statement not provided by supplier. See Kilmartin, J. V., B. Wright, and C. Milstein, 1982, J. Cell Biol., 93:576-582; Wehland, J., M. C. Willingham, and I. V. Sandoval, 1983, J. Cell Biol., 97:1467-1475; and, Wehland J, and Willingham MC, 1983, J. Cell. Biol., 97; 1476-90.

Eukaryotic cell lines

Policy information about [cell lines and Sex and Gender in Research](#)

Cell line source(s)

ExpiSF9 cells (Life Technologies, catalog #A35243)

Authentication

Authentication by supplier.

Mycoplasma contamination

Tested negative for mycoplasma contamination by manufacturer (tested using qPCR).

Commonly misidentified lines
(See [ICLAC](#) register)

No commonly misidentified cell lines were used throughout this study.